PCCP

The key role of the central cavity in sodium transport through ligand-gated Two-Pore Channels

Journal:	*Physical Chemistry Chemical Physics*
Manuscript ID	CP-ART-06-2021-002947.R2
Article Type:	Paper
Date Submitted by the Author:	n/a
Complete List of Authors:	Milenkovic, Stefan; Universita degli Studi di Cagliari, Physics Bodrenko, Igor; Istituto Officina dei Materiali Consiglio Nazionale delle Ricerche, CNR-IOM Cagliari Carpaneto, Armando; Università degli Studi di Genova, Department of Earth, Environment and Life Sciences (DISTAV); Ceccarelli, Matteo; Universita degli Studi di Cagliari, Physics; CNR, IOM Unita di Cagliari

The key role of the central cavity in sodium transport through ligand-gated Two-Pore Channels

Stefan Milenkovic[a], Igor V. Bodrenko[b], Armando Carpaneto[c], Matteo Ceccarelli[a,b,*]

[a]Department of Physics, University of Cagliari, 09042 Monserrato, Italy
[b]Istituto Officina dei Materiali – Consiglio Nazionale delle Ricerche, Unità di Cagliari, 09042 Monserrato, Italy
[c]Department of Earth, Environment and Life Sciences (DISTAV), University of Genoa, 16132 Genova, Italy

* matteo.ceccarelli@dsf.unica.it

Abstract

Subcellular and organellar mechanisms have manifested a prominent importance for a broad variety of processes that maintain cellular life on its most basic level. Mammalian Two-pore channels (TPCs) appear to be cornerstones of these processes in endo-lysosomes by controlling delicate ion-concentrations in their interiors. With evolutionary remarkable architecture and one-of-a-kind selectivity filter, TPCs are an extremely attractive topic *per se.* In the light of the current COVID-19 pandemic, hTPC2 emerges to be more than attractive. As a key regulator of the endocytosis pathway, it is potentially essential for diverse viral infections in humans, as demonstrated. Here, by means of multiscale molecular simulations, we propose a model of sodium transport from lumen to cytosol where the central cavity works as a reservoir. Since the inhibition of hTPC2 is proven to stop the SARS-CoV2 *in vitro,* shedding light on the hTPC2 function and mechanism is the first step towards the selection of potential inhibiting candidates.

Introduction

Two-pore channels (TPCs) consist of three proteins (TPC1-TPC3) and are part of a large superfamily of voltage-gated ion channels[1] present in eukaryotes. These homodimers are composed of two subunits and each of them consists of two homologues Shaker-like 6 transmembrane domains. Due to this architecture, TPCs are believed to be evolutionary milestones between four-domain monomer ion channels and homotetrameric ion channels.[2] Importance of TPCs' functions in mammals and plants is unquestionable since they take part in numerous physiological processes: nutrient metabolism,[3] lysosomal/vacuolar morphology and pigmentation,[4,5] autophagy[6] and neonagiogenesis.[7,8] Moreover, their active participation in the transport of cations potentially assigns to them the control of resting potentials and pH in endolysosomes.[9] This function is key for the endo/exocytosis processes, and TPC channels have been indicated as strongly involved in the mechanism of infection of diverse viruses, such as EBOLA,[10] Mers-CoV[11] and, recently, the large coronavirus family, particularly SARS-CoV and SARS-CoV-2.[12–14]

Regardless of their wide importance, the comprehension of TPCs as intracellular ion channels has been lagging behind when compared to their plasma membrane counterparts. The main reason for such an imbalance in the research focus was the unapproachable nature of the TPCs, both physiologically and structurally. Just in the last years TPCs were introduced to the computational biophysics community by employing techniques such as X-ray crystallography,[15,16] cryo-EM[17–19] and expression in heterologous systems.[20–22] The current state of knowledge identifies mammalian TPCs as Na^+-selective channels activated by the binding of phosphatidylinositol 3,5-bisphosphate [PtdIns(3,5)P_2],[7,23,24] with TPC1 showing a voltage dependence[17] and an activity that is modulated by the Ca^{2+} concentration.[7] A functional analysis

of mutation sites combined with docking studies on homology models discovered the presence of a specific lipid-binding pocket in human TPC2,[23] whereas electrophysiological experiments and modelling of TPC2 indicate that the small hydrophobic molecule naringenin can inhibit some of its functions.[7,25,26] Moreover, it was shown very recently that naringenin can inhibit Covid-19 infection *in vitro.*[12,13] It is worth noting that in plants TPC1 is a cation-selective,[27] Ca^{2+} permeable,[28,29] voltage-gated channel whose activity doesn't depend on PtdIns(3,5)P_2[21] but demands increase in cytosolic calcium instead.[15] This broad cationic selectivity can be narrowed down to Na^+ only, by means of mutagenesis thus mimicking the mammalian one.[16]

Cryo-EM studies of the mTPC1[17] (Figure 1A) and hTPC2[18] (Figure 1B) confirm that the mammalian TPCs pore has an aspargine-dominated selectivity filter (SF) on the lysosomal side, a feature unseen in other sodium channels where charged residues are present,[2] see Fig. 1. Furthermore, in TPC2 the selectivity tendency for either calcium or sodium was reported to be controlled by agonist binding molecules making TPC channels different from other ion channels again.[30,31] However, one should note that although having the same SF, mTPC1 and hTPC2 display some modest differences. For example, in contrast to mTPC1, the cryoEM structures do not resolve hTPC2 with sodium in the SF. Also, we observe that the SF of hTPC2 appears to be slightly narrower, which may be a reason behind the lack of a sodium ion inside the SF in hTPC2 (or *vice versa*).

Below the SF region a considerable volume of space, the central cavity (CAV), is lined by a fine mixture of hydrophobic and polar (non-charged) aminoacid residues and it is expected to be occupied by water molecules to hydrate diffusing ions. The CAV's boundaries are two pairs of six transmembrane helices S6, one per subunit. In both TPC1 and TPC2, PtdIns(3,5)P_2 molecules bind exclusively to the first domain (the binding site is situated at the junction formed by S3, S4

and the S4–S5 linker of DI[18]) while only S4 in DII (not in DI) responds to voltage changes in TPC1; TPC2, despite being structurally similar to TPC1, behaves as a voltage-independent channel[21]. On the cytoplasmic side, the CAV is limited by a narrow hydrophobic constriction region known as the hydrophobic gate (HG) (Figure 1A) which modulates the pore activity. It is crucial to mention that according to the structural information, the hydrophobic gate in TPCs consists of two rings, each containing four hydrophobic residues, whereas in voltage-gated, plasma-membrane sodium channels (Na*v*) it has only one ring of four hydrophobic amino-acid residues. This additional hydrophobicity imposes a significant barrier for the sodium transport, which is the probable cause for low conductances, i.e. low flux rates in animal TPCs.[32] The concept of hydrophobic gating itself[33–35] and its importance for mTPC1 were examined in detail, showing how the binding of PtdIns(3,5)P_2 can increase the amplitude of the HG fluctuations, and together with partial desolvation of the sodium hydration shell, allowing for sodium transport to occur.[32] The range of the aforementioned fluctuations can vary significantly and although we have identified mTPC1-PtdIns(3,5)P_2 complex as activable by observing transport in enhanced molecular dynamics metadynamics (MTD) simulations, the transport of the sodium ions under a physiological transmembrane voltage was never detected. The reason probably lies in the voltage dependence of TPC1, as standard MD simulations are unable to capture the conformational rearrangements occurring in voltage sensing domains induced by the external voltage applied, likely to be in the order of hundreds of microseconds.[36] For extensive reviews on the structure, activity and pharmacology of TPCs please see.[19,37]

In this paper, we have investigated dynamics and function of hTPC2 which was selected for an extensive multi-scale study for two reasons: (i) it is only ligand gated, which should allow the simulation of ion diffusion in the fully open state of the channel with an applied external voltage,

and (ii) according to the literature, and in light of current events, it could have a striking physiological importance, as its inhibition is able to stop SARS-COV-2 infections *in vitro*.[13,26] The latter candidates the hTPC2 as a key target for developing new inhibitors that should help mitigating the current COVID-19 pandemic.

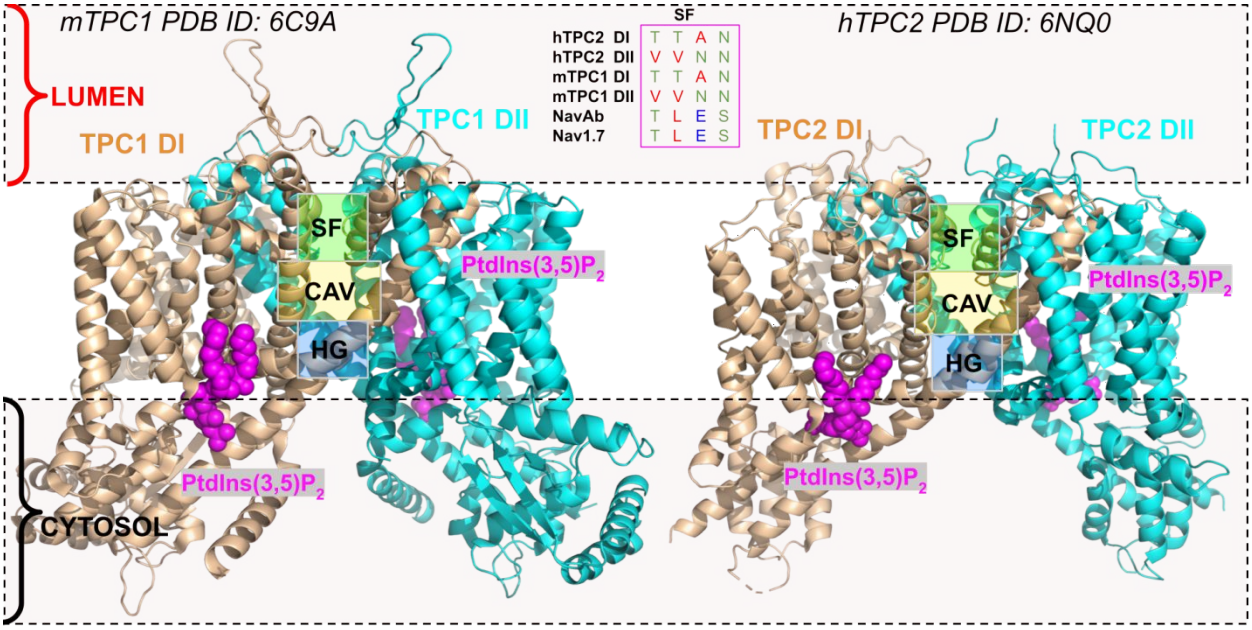

Figure 1. Cryo-EM structures of the mTPC1 and hTPC2[17,18] with indicated regions of importance: selectivity filter (SF), central cavity (CAV) and hydrophobic gate (HG). Top: comparison of residues at SF after alignment of dimeric TPCs and homotertameric Nav channels.

Results

MD simulations. Our models are based on the three recent cryoEM structures of TPC2, respectively with the protein in (i) closed apo state (apoC) , (ii) closed holo state (holoC, ligand bound), and (iii) open holo state (holoO, ligand bound).

Table 1. A summary of standard MD simulations performed.

System	PtdIns(3,5)P_2	Repeats	Time (ns)	Total time (ns)
apoC	no	10	300	3000
holoC	yes	10	300	3000
holoO	yes	10	300	3000

Each hTPC2 structure served as a template for 10 independent MD simulations, 300ns each, totalling 9 μs of sampling (3 μs per system.) (Table 1). Along these trajectories we performed the Cα-Cα cross-correlation analysis in order to establish a possible connection between the presence of the ligand and functional states of the dimeric protein matrix. In SI1 we can visualize the intensity of correlation in the three systems across all independent trajectories. We note several simulations with very strong (<-0.6) anti-correlation that couples the two subunits in holoO. In holoC that number is reduced to only one whereas in apoC it is non-existent. These results are summarized in SI2, where the total correlation per system was plotted against the corresponding Cα-Cα distance. In holoO simulations we observe the existence of two regions of distant highly (anti-)correlated residues. The regions are marked with black and magenta rectangles, for anti-correlated and correlated interactions respectively. These regions are non-existent or negligible, respectively in apoC and holoC simulations. We argue that this could mean that in holoC simulations effects of the PtdIns(3,5)P_2 binding are not notable yet, or that PtdIns(3,5)P_2 -bound state interconverts between open and closed state, characterized with a different subunit dynamics, as we have demonstrated for mTPC1.[32] Our assumptions can be backed up with the average pore radii distribution over the different simulations. In figure SI 5, one can see that there is a clear difference in distribution of the average pore radii among the three systems, but even in holoO simulations, the pore can be completely occluded.

The TPCs architecture shows the existence of a substantial central cavity, connecting the SF on the luminal side to the HG on the cytoplasmic side, occupied by water molecules. In order to understand the nature and dynamics of the central cavity we have analysed our simulations to calculate the average number of ions residing in the cavity. Though in the hTPC2 CryoEM structures we do not see resolved ions inside the cavity (two sodium ions are present in the mTPC1 CryoEM structure, respectively in the SF and CAV), we have identified three possible states: *i)* empty *, ii)* one sodium ion and *iii)* two sodium ions, as shown in Figure 2A. Moreover, we have calculated average residence times for each state of the cavity in all three systems and we have summarized them in Figure 2B. These residence times have been obtained as periods of time that CAV spends in a certain state before that state changes. We observe that the longest times (from 3 to 6 ns) correspond to having an empty CAV in the two closed structures, while in holoO open structure the longest residence time belongs to the state with one ion inside the CAV. On the other hand, the state with two ions in the CAV shows subnanosecond average lifetimes, suggesting a transient nature of this state.

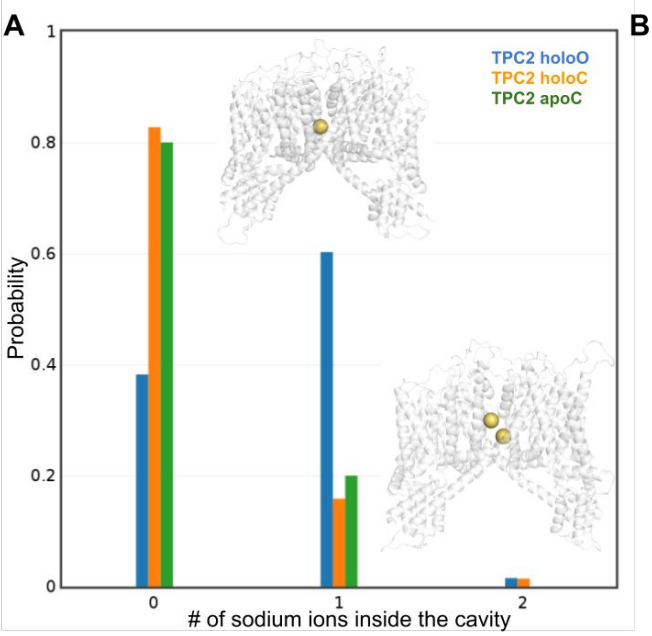

Simulation setup	τ_0(ns)	τ_1(ns)	τ_2(ns)
TPC2 holoO	2.2	3.04	0.46
TPC2 holoC	6.06	0.92	0.26
TPC2 apoC	5.41	1.8	0

Figure 2. A) Probability distribution of the sodium occupancy in the central cavity as obtained from plain MD simulations. TPC2 holoO, TPC2 holoC, and TPC2 apoC data are shown in blue, orange and green, respectively.* B*) Average residence times of CAV's different occupancy states for the three systems

Transmembrane voltage simulations. We performed MD simulations with a constant external electric field[38] to estimate the conductance of the channel. We have applied −200 mV, (V_{cyt} – V_{lumen}), a larger value than the expected physiological one of about -20:-40 mV,[39] on the 10 holoO systems for 300 ns each, registering on overall 11 passages. After that, one simulation was prolonged to 3μs, detecting 9 passages (Table 2). In both approaches, two different modes of sodium transport were observed, referred to as **fast** and **slow** and depicted in Figure 3.

Table 2. A summary of MD simulations performed under a transmembrane voltage.

System	Voltage	Repeats	Time (ns)	Total time (ns)	#of passages	Conductance (pS)
holoO	-200mV	10	300	3000	11	2.9
holoO	-200mV	1	3000	3000	9	2.4

In the fast mode two scenarios are possible (Fig. 3A-B), either *i)* a sodium ion enters the cavity and after another sodium ion reaches the selectivity filter, the first one leaves the cavity, or *ii)* a sodium ion is in the cavity when it is joined by a second sodium ion, they exchange their positions inside the cavity and the latter leaves. The slow mode operates with a sodium ion that penetrates into the empty cavity where it resides for a certain amount of time before leaving (Fig. 3C). These results clearly suggest that the kinetics of the sodium transport in hTPC2 depends on the given occupancy of the central cavity. In contrast to the known majority of studies where almost the entire interplay of sodium transport happens inside the SF and employs multiple strong binding sites,[40–44] we observe that sodium in our simulations passes through the SF in a relatively fast manner and it is not accompanied by another sodium ion.

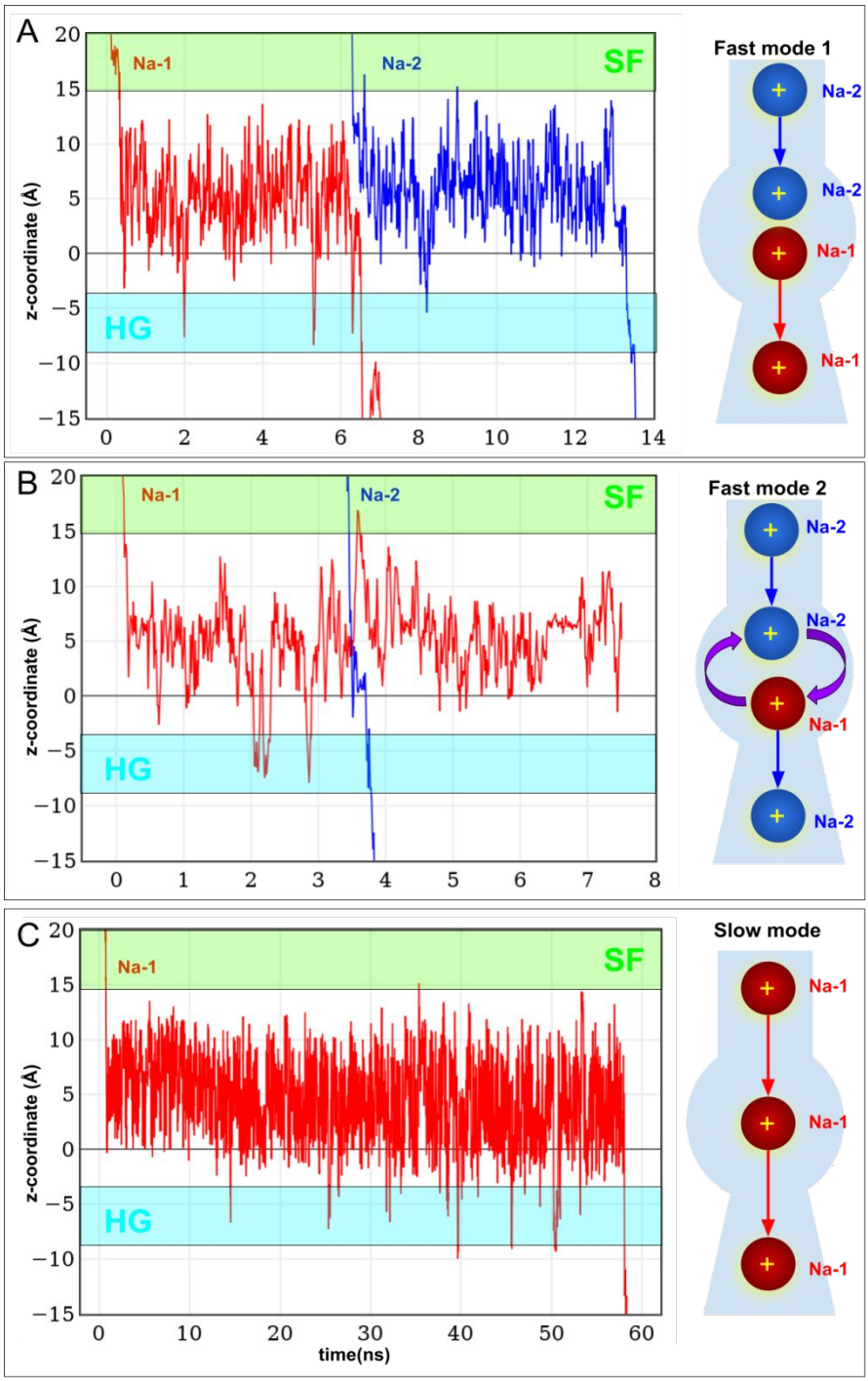

Figure 3. Different modes of sodium transport in hTPC2 as found in MD simulations with an external electric field. (A-B) Time series of z-axis coordinates of sodium ions in fast modes accompanied by

schematic representations on the right. C) Time series of z-axis coordinate of the sodium ion in the slow mode accompanied by a schematic representation on the right.

Most of the action occurs in the CAV, which appears to have a role of a peculiar reservoir and allows for a non-single file transport to occur. When we say non-single file transport, we think of a sodium ion that can move through the pore in a non-concerted manner, i.e. without some strict order that involves other ions.

MTD simulations. The low conductance of a single mammalian TPC (a few pS) does not allow to get more statistics and verify the permeation model with standard MD simulations,[32] as was done for potassium channels.[45] To demonstrate the existence of different occupancy states of the cavity by sodium ions and elucidate their role in permeation, we have run an extensive set of biased simulations, employing multiple walker MTD simulations, as shown in Table 3. We have modelled different states of the cavity by controlling its occupancy with position-restraints on sodium ions, keeping the cavity either (i) empty, (ii) with one, or (iii) with two sodium ions inside. A fourth system was prepared as a control simulation, without any restraints whatsoever. Because the lysosome is known to have calcium ions in its interior,[46] we also prepared a fifth system with a single Ca^{2+} ion restrained inside the cavity. For all these systems, we biased one single sodium ion forth and back from the cytosol to the lumen in order to obtain the free energy as a function of its position, as shown in Fig. 4.

Table 3. Summary of MTD simulations and free-energy difference for sodium transport between different regions of hTPC2. See SI for calculation of the error.

Simulation	length (ns)	CAV occupancy	**MTD Error** (kcal/mol)	**ΔG(HG-BULK)** (kcal/mol)	**ΔG(HG-CAV)** (kcal/mol)	**ΔG(SF-CAV)** (kcal/mol)	**ΔG(SF-BULK)** (kcal/mol)
MTD	~21,600	control	**1.3**	**~6**	**~10**	**~7**	**~3**
MTD_0	~19,200	0 x Na^+	**1.0**	**~4.5**	**~12**	**~8.5**	**~1**
MTD_1	~19,200	1 x Na^+	**0.9**	**~6**	**~5.5**	**~2**	**~2.5**
MTD_2	~10,000	2 x Na^+	**1.1**	**~9.5**	**~5**	**~3**	**~7.5**
MTD_{Ca2+}	~17,500	1 x Ca^{2+}	**1.3**	**~7**	**~3.5**	**~1.5**	**~5**

All the profiles show a central binding site separated from the cytosol and the lumen by two barriers, resembling the two-barrier one-binding site model,[47] developed in the '90 to rationalize the transport of molecules through specific porins. We observe a strong dependence on the cavity state, which occupancy modulates the strength of the central binding site. When the cavity is kept empty (blue line), the moving sodium experiences a deep binding site, MTD_0. This results in high energy barriers for escaping the cavity (Table 3), either through the SF or the HG and corresponds to the slow mode detected in the external electric field simulations (Figure 3C). On the other hand, when the cavity is permanently occupied by one ion, the central binding site is not strong, and the barriers to escape either through the HG or the SF are reduced, MTD_1. In particular, the energy barrier to escape through the HG is reduced by 7 kcal/mol relative to the empty cavity, MTD_0, and we can draw a clear analogy with the fast modes described in Figure 3A-B.

If we increase the number of sodium ions permanently present in the cavity to two, the free energy needed for escaping the cavity remains the same relative to the MTD_1 but the energy needed for entry from both the lumen and the cytosol increases significantly (> 3.5 kcal/mol), suggesting low probability for such a scenario. We note that the system with no bias on the cavity occupancy (Figure 4, purple line) has a free-energy profile that lies between the MTD_0 (blue line) and MTD_1 (green line) in the CAV region. This resembles well the pure MD results, obtained with a Na concentration of 150mM, that find the cavity most probably in one or another state depending on whether or not the channel is open or closed.

Qualitatively our results do not change if we use another estimator for the free energy surfaces of Figure 4A, as explained in SI and reported in Fig. SI4.

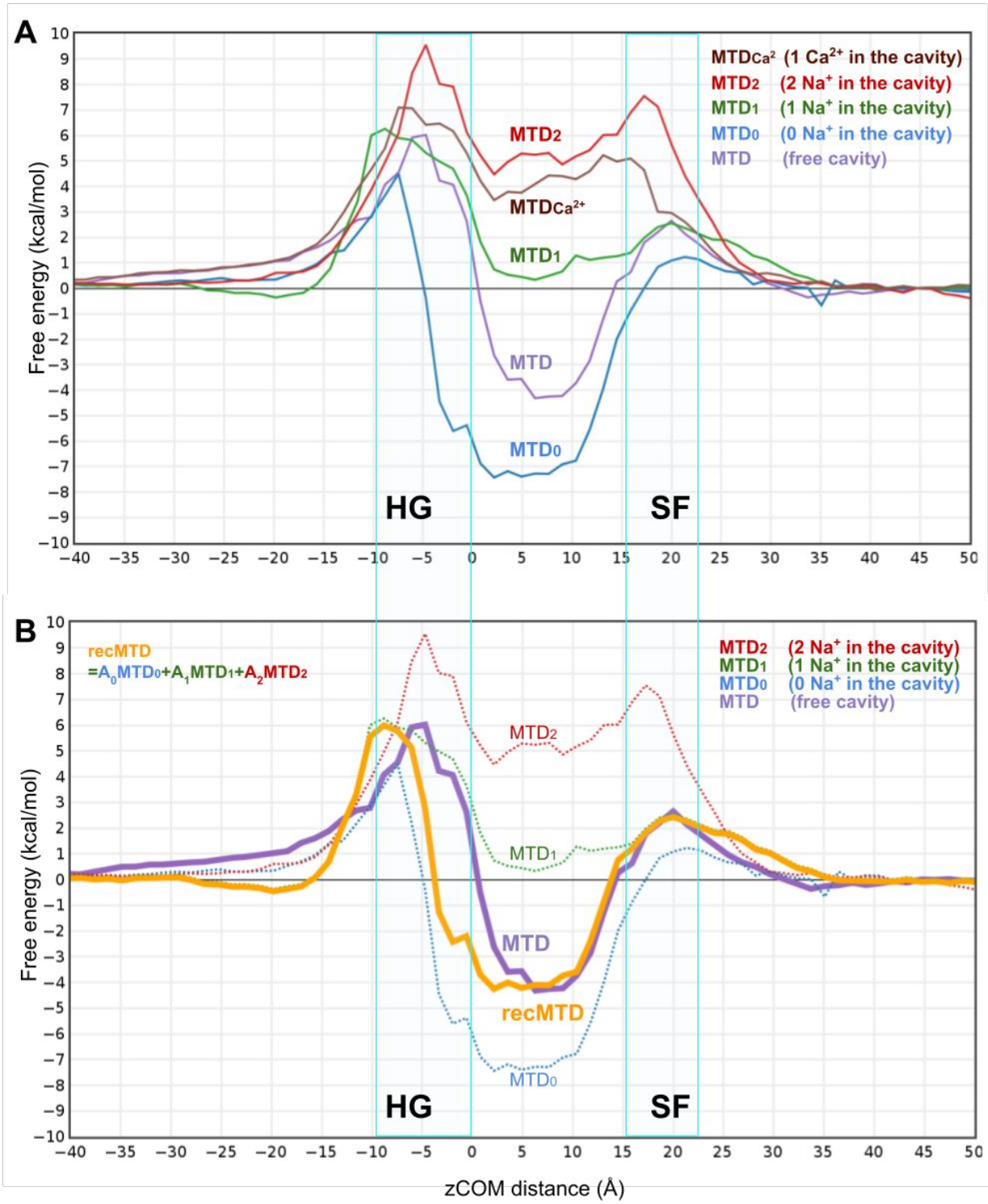

Figure 4. A) Free energy profiles obtained from different MTD simulations. B) Reconstruction of the free cavity MTD simulation FES profile (violet) by combining three independent MTD simulations:

MTD_0 and MTD_1 and MTD_2 shown in blue, green, and red, respectively. The reconstructed profile is shown in orange.

The cavity state seems to have very interesting effects on both HG and SF regions. The effects of having a cavity with zero or one sodium ion inside during the transport creates a symmetric low increase in both barriers of the aforementioned regions relative to the bulk. However if a single Ca2+ ion is placed in the cavity the situation changes: the barrier on the HG is not strongly affected (~1 kcal/mol), suggesting that two rings of hydrophobic residues are enough to screen the electrostatic interactions of Ca2+. On the other hand the SF barrier rises up by 2.5 kcal/mol. When 2 sodium ions occupy the cavity we see an increase of both barriers with respect to the case with one Ca2+, which proposes that the distribution of charges also plays an important role, not only it's absolute value. Therefore we have investigated the most probable occupancy sites inside the entire pore, though we did not observe regions of strong interactions. In the case of the calcium ion, we have obtained a distribution that suggests that calcium can occupy three distinct positions: (i) the beginning of the SF; (ii) the end of the SF and (iii) inside the central cavity as shown in Figure 5A. The latter can be understood as a single occupancy site that has a three fold degeneracy, as it can be decomposed into three Gaussian distributions. This interpretation agrees well with the picture that can be seen in the calcium conducting channels where similar observations are made by X-ray[48,49] or by molecular simulations.[50] More precisely, Saotome et al.[49] predicted the three most probable positions of a calcium ion to be i) at the beginning of the SF, ii) at the end of the SF, and iii) in the middle of CAV, with the distance between neighboring positions being 0.79 nm and 0.68 nm respectively. In our case, the most probable positions of the calcium have zCOM value of 2.1 nm (SF beginning), 1.4 nm (SF end) and three CAV positions at 0.9nm, 0.6nm and 0.3 nm with the one at 0.6 nm being the representative. This gives us the

neighboring distances of 0.7nm and 0.8nm which, as we said, matches well the situation observed in calcium transporting channels.

When we have only one sodium ion we again see three sites inside the cavity (0.2, 0.5 and 0.8 nm), and one just outside the SF (1.2 nm). Sodium has an additional site in the HG region (-0.1 nm), not seen with calcium due probably to the different size of the hydration shell (Figure 5B). When we place two permanent sodium ions inside the cavity, we see the three internal sites more spaced and an additional 6th site at the beginning of the SF region, observed already for calcium (Figure 5C).

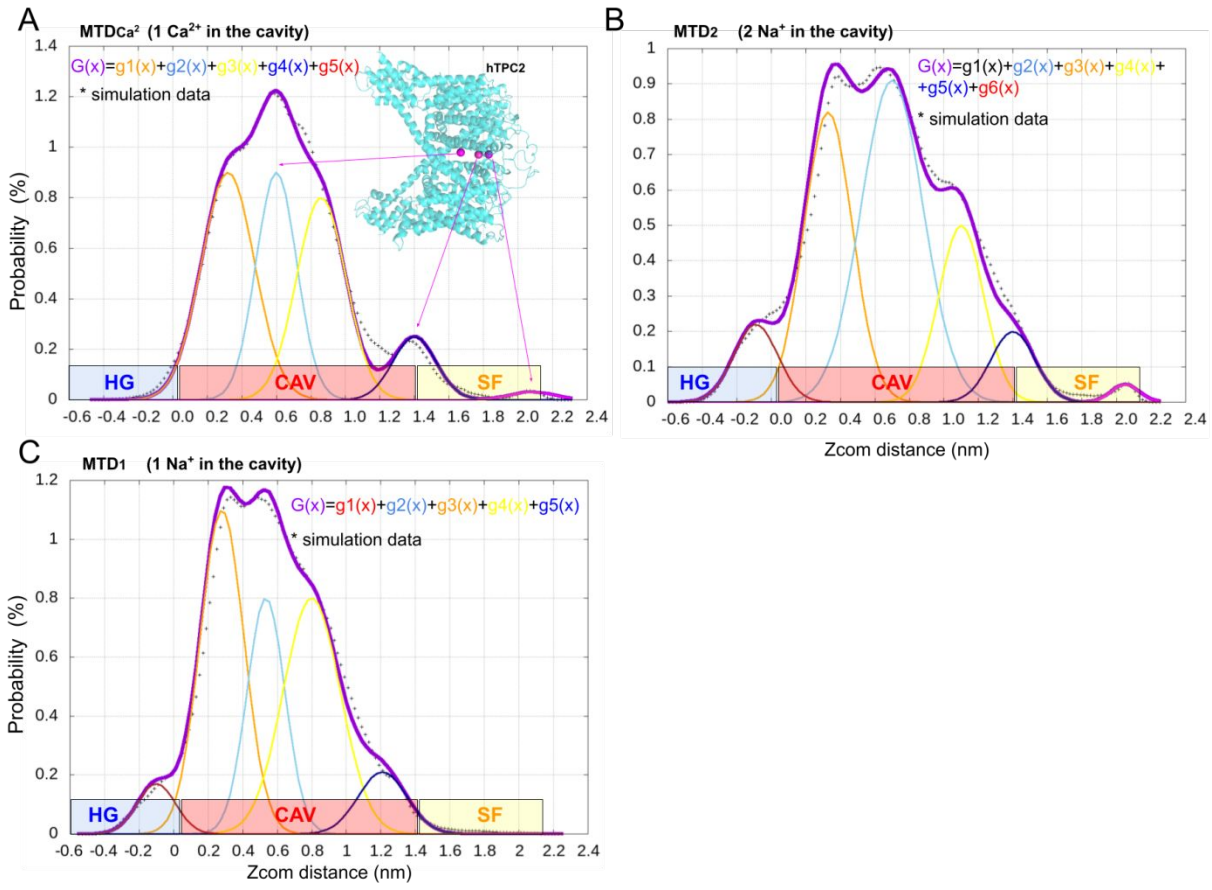

Figure 5. A) A decomposition of the Ca^{2+} position probability during the MTD_{Ca2+} simulation inside the channel into gaussian components shows discretization of most probable positions. The simulation data are shown as black crosses. Three selected positions are shown in the molecular graphics inset as

vdW spheres. B) A decomposition of the Na^+ position probability during the MTD_2 simulations inside the channel into gaussian components shows discretization of most probable positions. The simulation data are shown as black crosses. C) A decomposition of the Na^+ position probability during the MTD_1 simulations inside the channel into gaussian components shows discretization of most probable positions. The simulation data are shown as black crosses.

To understand the nature and significance of the detected sites, we took a step back and calculated the ion density in the case of the holoO -200mV simulations. This distribution was then used to get a free-energy profile which was corrected for the presence of the external electric field, as described in ref [51]. Figure 6 shows an overlap of the holoO -200mV ion density based free energy with MTD_0 , MTD_1, and MTD_2 profiles. We see that the free energy profile extracted from the simulation with the external electric field matches best the MTD_1 profile suggesting that under the given concentration of 150 mM, the single CAV occupancy is optimal for sodium transport. We do observe a certain discretization of the SF barrier which can be interpreted as binding sites of a modest strength, in agreement with the sodium distribution observed in MTD simulations. Interestingly, these binding sites are completely non-existent in the regular MD simulations suggesting that their presence is triggered by the external electric field. In addition, we confirm that the HG region appears to be a main bottleneck also with the transmembrane voltage on.

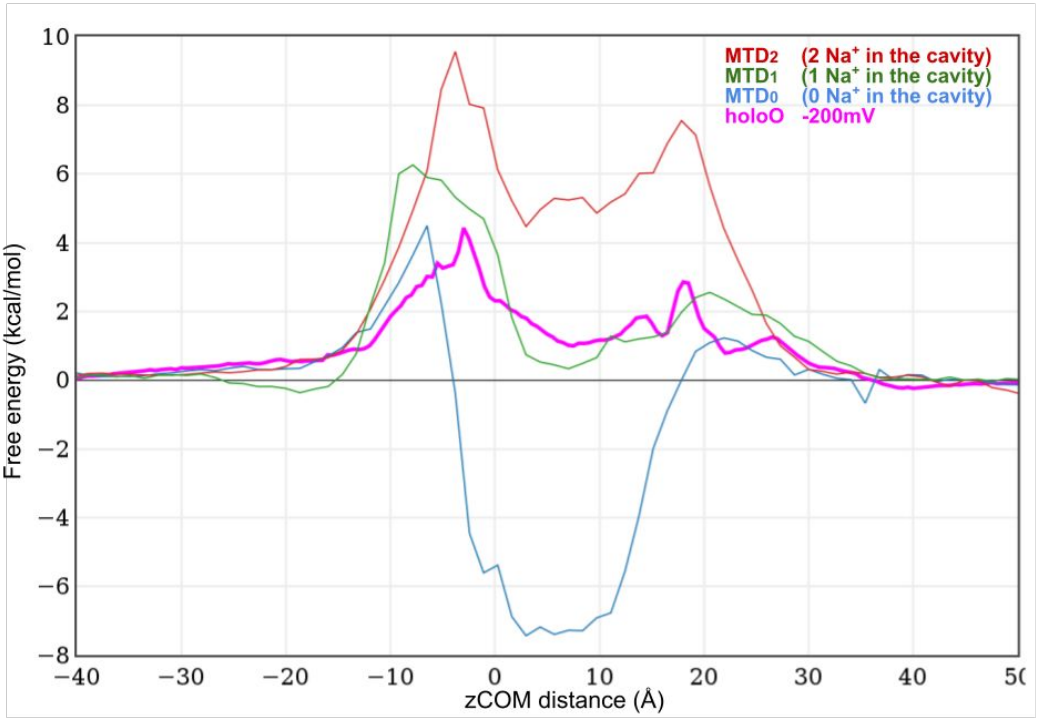

Figure6. The overlap of the free-energy profiles extracted from holoO -200mV (magenta) simulations and MTD simulations with CAV occupancy controlled.

One would also expect that the control MTD free-energy profile can be obtained by reweighting the free-energy profiles of the restricted simulations with 0, 1 and 2 Na+ ions inside the CAV:

$$recMTD = A_0 \cdot MTD_0 + A_1 \cdot MTD_1 + A_2 \cdot MTD_2$$

After taking into account the corresponding statistical weights and relative occupancies, we have obtained the three coefficients A_0, A_1, and A_2. The recMTD (orange line in Fig. 4B) has a nearly perfect overlap with the control MTD simulation (violet line in Fig. 4B) (See SI for derivation). This overlap shows all-around consistency of methods applied and allows us to continue with estimation of the macroscopic flux properties from the free energy profiles.

Ion Current estimation. The free-energy profiles determine both the equilibrium probabilities for an ion to occupy a certain region of the channel and the ion current through the channel driven by the concentration gradient or an external electric field. We employed a theoretical

method that combines the diffusion equation and the Markov state model to estimate the current of ions over a FES, driven by the external ion concentration gradient.[52,53] We have already applied this approach to predict the current of molecules through porins as a function of gradient concentration.[54,55] The combination of the two kinetic models allows one to take into account both the diffusivity nature of ions during transport and internal binding that can provide saturation in the current, depending on external concentration. The free-energy profile for an ion contains the interaction with the channel residues, with the solvent as well as the effective local mean field created by all the other ions, and therefore, it depends on the local ion concentration. The internal occupation depends on external ion concentration, so one would need to calculate the free energies at different ion concentrations. That would require several times more computational resources we consumed which are already quite substantial. Instead, for a qualitative analysis, we used the computed restricted free energies, $MTD_{0\text{-}2,}$ to estimate the ionic (particle) current from CIS to TRANS (from lumen to cytosol) driven by the gradient of concentration as a function of increasing external ion concentration (the ions are added to the CIS side only).

At low concentration, when presumably CAV is not occupied permanently, the low barriers we found in MTD_0 allow for the highest possible current. This current is predicted of the "Fick's type" (linear with the concentration gradient) up to the concentration of 1 μM, when the presence of the deep central binding site creates the saturation of the current (as only one ion is allowed to occupy the CAV region). However, in this condition we expect to have the cavity permanently occupied, thus the kinetics would follow instead the MTD_1 curve. With the CAV occupied permanently by one ion, we predict higher current from 10 μM and no saturation till 0.1 M, a value close to the expected concentration of sodium in lysosome (110 mM).[56] It is interesting

also to note in Fig. 7 how this curve is similar to the current of sodium obtained with one calcium ion inside the cavity. On the other hand, at high sodium concentration, when the cavity might be occupied by two sodium ions, the current is very low (Figure 7).

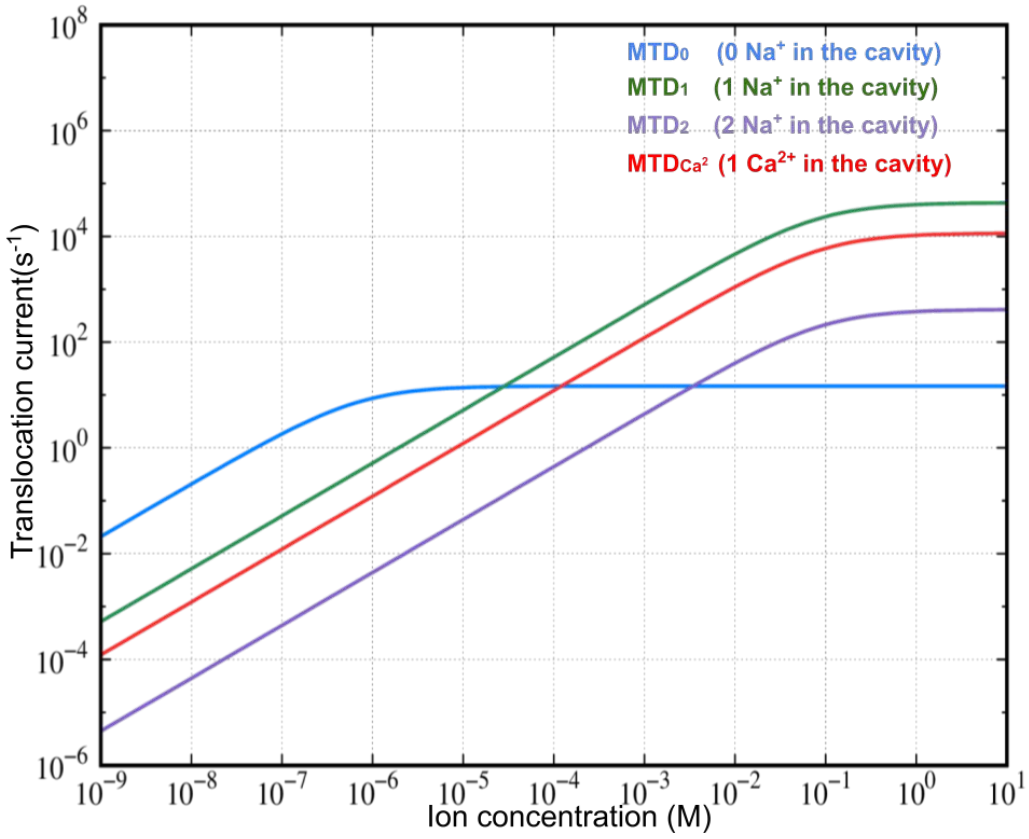

Figure 7. Translocation current dependence on ionic concentration gradient for MTD_0 (blue), MTD_1 (green), MTD_2 (purple) and MTD_{Ca2+} (red).

Discussion

A systematic MD investigation of the hTPC2 dynamics, based on three cryo-EM structures,[18] shows that upon PtdIns(3,5)P_2 binding hTPC2 can exhibit significant anti-correlated motions between the subunits, depending on whether or not the pore is found in open or closed state. This behaviour has been previously observed in the case of mTPC1 suggesting it to be a property peculiar to the mammal TPC channels.

Our extensive multi-scale study of the hTPC2 further employed the external electric field simulations and MTD simulations, in which we have successfully modeled the flux of sodium ions through the PtdIns(3,5)P_2-bound hTPC2 in the open conformational state. This allowed us to observe multiple complete passages of sodium ion, from the lumen to the cytoplasm, crossing the SF, the CAV, and the HG. Our observations started with identification of different CAV states with respect to the number of sodium ions staying in it and their respective residence times. The calculated residence times of the CAV states highlight a diverse kinetics of sodium ions, which is confirmed by the analysis of sodium paths from the lumen to the cytosol. hTPC2 appears to feature three modes of conduction for sodium ions, namely one slow and two fast modes. We should mention that some modes of sodium transport reported here do qualitatively resemble some of the already proposed mechanisms.[48–50] In particular, the first fast mode (Figure 3A) is similar to the knock-off mechanism introduced for the diffusion of calcium ions. However, as we have already stated in our description of sodium transport in hTPC2, the main stage belongs to the CAV, which differs from previously proposed mechanisms in other ion channels. For an excellent overview of the proposed mechanisms of ion transport one should see ref [57].

We believe that this is connected to the fact that the SF of the TPCs is unique in the world of sodium channels with no charged residues whatsoever (Fig.1). It is worth noting that we present here a complete diffusion of sodium ions, from the luminal side to the cytosol, in contrast to most of the previously reported simulations that for various reasons were focusing on the SF and its vicinity, only. Nevertheless, the ideas of binding sites and pore saturation will remain valid but in this case for the entirety of the pore.

According to our results, the mechanism proposed for transport of sodium ions through hTPC2 has several distinctive features: (i) we do not see strong binding sites in the SF region; (ii) the central role in the transport belongs to the CAV; (iii) the calculated ion density suggests the existence of several "preferential" positions inside the pore. The cause for such a behavior appears twofold: i) SF of the TPCs lacks well defined binding sites, and ii) the main barrier in all simulations performed on hTPC2 and including our previous work on mTPC1 is the HG region. This barrier will control the sodium transport and can keep them diffusing inside the CAV whereas TPCs' SF lacks charged residues that would allow strong local interaction of the sodium-hydration shell system with the protein. The loose coordination of sodium ions was already put forward.[57] From the model point of view, the binding site idea seems to hold but the binding itself occurs in the CAV at precisely set positions and with well-defined energetics, as our reconstructed free-energy profiles suggest.

Further, with our multiscale Markov-state approach, we analysed the reconstructed free energies to obtain the current of ions depending on the occupancy of CAV. The number of sodium ions in the CAV modulates the kinetics of the sodium transport by changing the energetics of the process; thus the CAV's multi-occupancy, verified with both standard and enhanced MD simulations, controls the transport of sodium by avoiding saturation at high concentrations: this interesting feature permits a 'Fick's type' current, a linear transport mechanism that allows hTPC2 to be operational in a wide range of gradient concentrations with the same efficiency. We also verified that the presence of a calcium ion inside the CAV does not change the current of sodium ions significantly, as already observed in a prokaryotic sodium channel.[58] Because the lysosome is also a reservoir for calcium (0.5 mM vs 110 mM of sodium),[56] its presence in the CAV might occur, however it would not interfere too much with sodium transport. Interestingly,

two sodium ions that electrostatically match one calcium ion appear to increase the transport barriers, which again suggests that the CAV occupancy indeed controls the sodium transport entropically.

It is interesting to combine the results on the multi-occupancy and the predicted values of saturated currents. Because the occupancy of the CAV is correlated to the external concentration of ions, our saturated currents (Fig. 7) having the maximum for one sodium ion inside the CAV This is a well-known feature of ion channels, which says that the conductance curve will increase with the concentration until it reaches its maximum after which any further increase in the external concentration would result in a decrease of the conductance thus resembling a bell shape. Long time ago Hille, without having any knowledge of the structure of ion channels, explained the bell-shaped curve of conductance as characteristic of a system with selective (and thus saturable) multiple binding sites.[59]

However, he concluded that this is not the only way to display the bell-shaped conductance behavior. In our case, though we do not see strong binding sites at the SF, the saturated currents have a bell-shaped trend. We argue that this is a consequence of a multi-binding site mechanism that occurs in the CAV and propose a model shown in Figure 8: the optimal transport at physiological concentration is achieved once the CAV is occupied by one sodium ion. This configuration yields the highest possible flux of ions for the given conditions by modulating the kinetics of the transport. We further argue that the CAV plays the central role in mammalian TPCs because the principle bottleneck appears to be the HG region even in the conformational states that are defined as open. This allows a particular accumulation of sodium to appear in the CAV. Additionally, lacking strong binding sites in the SF strengthens CAV's dominant position in the entire process.

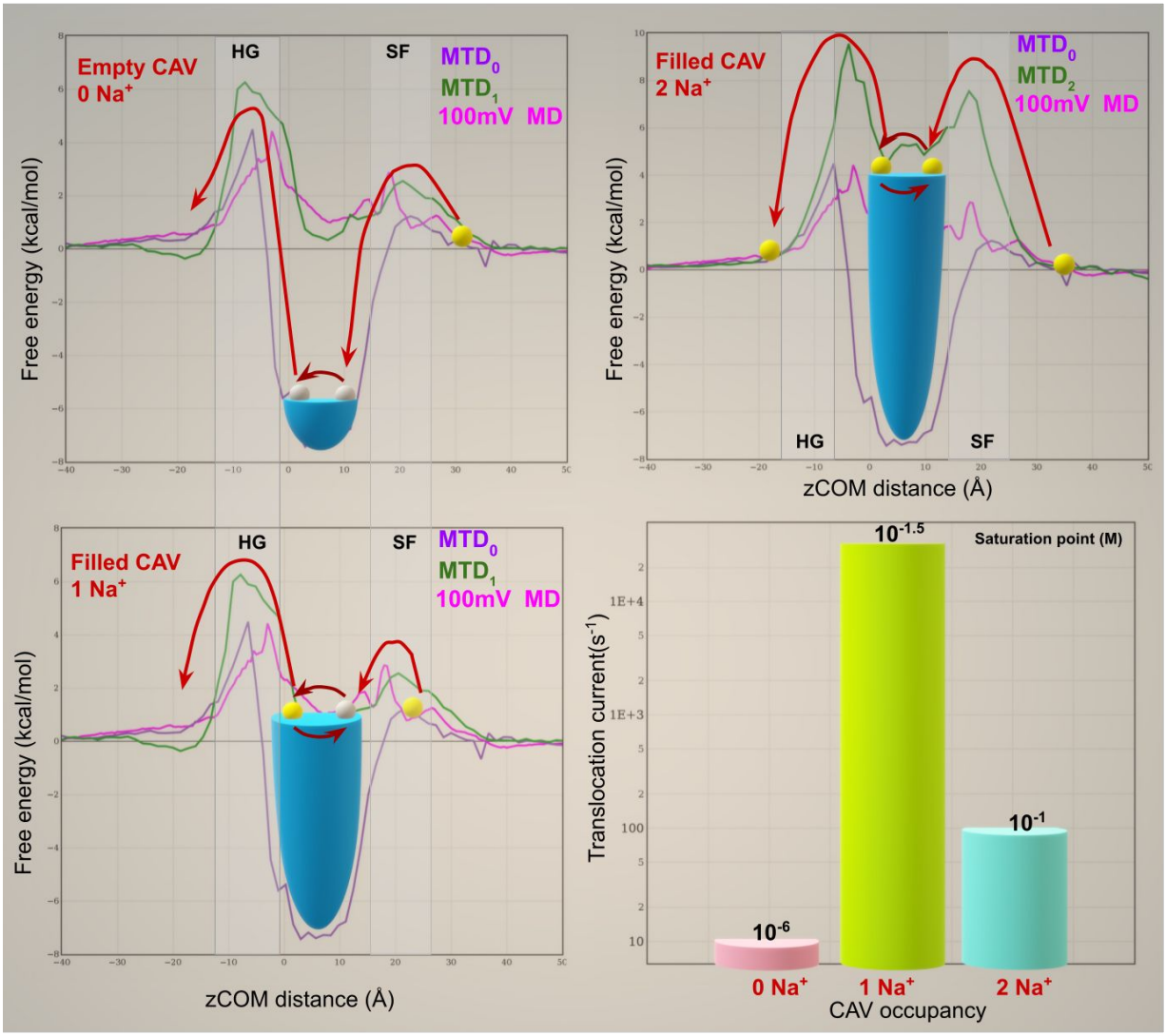

Figure 8. Models of sodium transport depending on the cavity state where sodium ions are depicted as yellow spheres and empty occupancy sites as grey spheres. A), B) and C) represent CAV with zero, single and double occupancy respectively. D) Translocation current estimated for each model with their respective saturation concentrations given in black.

In summary, we elucidated the mode of transport for sodium ion in hTPC2, characterized by a loose SF, a multi-occupancy central cavity, and a strict HG controlled by a ligand. This represents a first complete model of hTPC2 sodium transport, a starting point to solve open questions regarding hTPC2 and to search for molecules that inhibit TPC2 functions.

Methods

All of the simulations we have performed in this work used three cryo-EM structures of hTPC2 as initial coordinates: without PtdIns(3,5)P2 in closed state (apoC), with PtdIns(3,5)P2 in closed state (holoC), and with PtdIns(3,5)P2 in open state (holoO) given with PDB IDs 6NQ2, 6NQ1 and 6NQ0, respectively. After the missing loops were built with GalaxyFill[60] the setup was continued by employing CHARMM-GUI web server. The first step was inserting the protein structure into the lipid bilayer[61,62] that consists of 521 POPC (1-palmitoyl-2-oleoyl-sn-glycero-3-phosphocholine) molecules forming an xy-plane sized 150Å × 150Å. The bilayer-protein complex was then immersed in an explicit water solution with Na^+Cl^- concentration of 0.15 M, for a total of 316508 atoms. The set of heating/equilibration/production files was provided by CHARMM-GUI[63,64] and it was performed using GROMACS.[65–70] We have used CHARMM36m[71–73] for protein with CMAP[74] correction for the backbone atoms. Lipid bilayer was built using CHARMM36 lipids[75] whereas for the water molecules we have used the TIP3P model.[76] For obtaining parameters for PtdIns(3,5)P2 we have used the CHARMM General Force Field[77] within CHARMM-GUI. We have used NPT ensembles where, during the equilibration, pressure and temperature were kept constant at 1 atm and 310 K, respectively, using the Berendsen coupling scheme.[78] During the production run we kept the same values for both pressure and temperature by employing Parrinello-Rahman coupling scheme.[79] A 12 Å cutoff was used for the list of neighbors, vdW and Coulomb force where vdW force was controlled by switching function centered at 10 Å. Electrostatic interactions were treated with the smooth particle-mesh Ewald technique.[80] Although they introduced some controversy for the potassium channels,[81] the updated nonbonded (NBFIX) parameters for sodium,[82] chloride[83] and calcium[84] were used to treat ionic interactions with the surroundings.

Simulations with the transmembrane voltage (V) were performed in the NVT ensemble by applying the external electric field (E) along the z-axis in a conventional way where each charged particle feels the force F=qE[38] and the external electric field equals E=-V/L_z where L_z is the size of the periodic cell along the field. In this way we apply a constant drop of potential along the desired axis which redistributes system ions in a manner that creates a realistic drop of potential at the point of the greatest resistance.[85]

The holoO setup was prolonged with the metadynamics in the NVT ensemble by combining the PLUMED-2[86] with GROMACS. For collective variables we have chosen the Z-component of COM distance between the protein and the biased ion (Z_{COM}), and the number of contacts between HG and water molecules (HG hydration number). Because of the differentiability the latter was given as a continuous switching function centred on 3Å where all the water molecules within the 5Å of the HG amino acid residues were considered. This function is implemented within the PLUMED with COORDINATION command with a functional form:

$$S_{i,j} = \frac{1-\left(\frac{r_{ij}}{r_0}\right)^n}{1-\left(\frac{r_{ij}}{r_0}\right)^m} \quad (1),$$

and the total number of the contacts achieved between HG (index *i*) and molecules of water (index *j*) is:

$$\sum_i \sum_j S_{i,j} \quad (2).$$

For n and m parameters of the switch function we take 6 and 12, respectively. Aforementioned collective variables were explored by distributing Gaussian-like potentials with 10 ps frequency

and with a width of 0.25 Å for the sodium position and 3 for the hydration number. The initial gaussian height was 1.0 kcal/mol and it was adjusted throughout the simulation by means of well-tempered metadynamics with the temperature set to 3000K.[87,88]

In metadynamics simulations with the fixed number of ions in the cavity, the restraints were applied on the z-component of the ion-protein COM distance, effectively set at the outer regions of SF and HG. As this is a relative distance, we do not need to change it during simulations. These restraints do not allow penetration of ions other than the biased one. Also, these restraints do not allow escape of the ions that are intended to be in the cavity for the entirety of the simulation. In order to evaluate the convergence of the free energy surfaces, we employed a different estimator[89] and we compared one-by-one the surfaces, as discussed more extensively and reported in SI.

To calculate the single-channel conductance for sodium ions we have employed the linear diffusion-drift approximation by solving 1D Smoluchowski equation in the small-voltage limit,[90]

$$G_0(c) = Pq^2 c\frac{F^2}{RT}S_c \qquad (3)$$

where P, q=1, and c are the permeability coefficient, the charge in atomic units and the molar concentration outside the channel equal on the both sides, respectively, for the ions; F is the Faraday's constant and R is the ideal gas constant; S_c is the geometric cross section at the mouth of the channel. For the permeability coefficient was have used the Kramers-type formula,

$$P = \left[\int_0^L \frac{\exp\left(\frac{U(z)}{kT}\right)}{D(z)} \right]^{-1} \qquad (4)$$

where, $U(z)$ is the potential of mean force (the free energy profile, see Fig R4) for the ion at position z (normalized to zero value outside the channel, $U(0) = 0$), $D(z)$ is the local diffusion constant, L, is the geometrical length of the channel. Besides, as the major contribution to the integral in Eq. (4) comes from the barrier region, we have assumed that the effective diffusion constant in the channel is position-independent, $D(x) = D_{eff}$, and set $D_{eff} = 1\text{nm}^2/\text{ns}$. The monomer channel cross section at the mouth was taken corresponding to the radius of 10 Å, and the channel length *L=62* Å. In the diffusion-drift approximation, (Eq. 3), the ionic conductance is linear with the particle concentration. The total average number of the ions in the channel (in the small-voltage limit) reads

$$N_i(c) = S_c N_A c \int_0^L \exp\left(-\frac{U(z)}{kT}\right) dz. \quad (5)$$

At small ion concentration, when $N_i(c) \ll 1$, this quantity has the meaning of the probability to find a particle in the channel. This latter interpretation allows one to bridge the diffusion-scale model with the 2-state Markov model of the particle-pore kinetics, as it was done for the concentration gradient driven current of molecules.[54,55] The 2-state Markov model assumes that only one particle at a time may occupy the channel and can describe both the linearity with the concentration and the saturated behavior when the ionic current becomes concentration independent. Then, the saturation-corrected conductance reads,

$$G_s(c) = \frac{G_0(c)}{N_i(c) + 1}. \quad (6)$$

The condition of a single ion at a time in the total channel may be too strong, so that $G_s(c)$gives a rather lower-bound estimate of the channel conductance. While the linear quantity, $G_0(c)$, gives the upper-bound estimate of the conductance.

The pore area dynamics was recorded calculating the area available to a probe of radius 1.4 Å rolling on a 3D grid with space 0.5 Å, using a home-made script which was already successfully applied to porins.[91]

SUPPORTING INFORMATION

The Supporting Information is a PDF file with 4 figures, SI1-SI4.

AUTHOR INFORMATION

Corresponding Author

*Matteo Ceccarelli, Department of Physics and IOM/CNR, University of Cagliari, 09042 Monserrato, Italy, matteo.ceccarelli@dsf.unica.it

Author Contributions

The manuscript was written through contributions of all authors. All authors have given approval to the final version of the manuscript.

ACKNOWLEDGMENTS

We acknowledge PRACE for awarding us access to Marconi100 at CINECA (Italy) through the COVID-19 Fast Track Call, project n. 48, and the 22nd call, project nr. 2020235493.

REFERENCES

(1) Frank, H. Y.; Catterall, W. A. The VGL-Chanome: A Protein Superfamily Specialized for Electrical Signaling and Ionic Homeostasis. *Sci. Signal.* **2004**, *2004* (253), re15.

(2) Rahman, T.; Cai, X.; Brailoiu, G. C.; Abood, M. E.; Brailoiu, E.; Patel, S. Two-Pore Channels Provide Insight into the Evolution of Voltage-Gated Ca2+and Na+ Channels. *Sci. Signal.* **2014**, *7* (352), ra109–ra109. https://doi.org/10.1126/scisignal.2005450.

(3) Cang, C.; Zhou, Y.; Navarro, B.; Seo, Y.; Aranda, K.; Shi, L.; Battaglia-Hsu, S.; Nissim, I.; Clapham, D. E.; Ren, D. MTOR Regulates Lysosomal ATP-Sensitive Two-Pore Na+ Channels to Adapt to Metabolic State. *Cell* **2013**, *152* (4), 778–790.

(4) Ambrosio, A. L.; Boyle, J. A.; Aradi, A. E.; Christian, K. A.; Di Pietro, S. M. TPC2 Controls Pigmentation by Regulating Melanosome PH and Size. *Proc. Natl. Acad. Sci. U. S. A.* **2016**, *113* (20), 5622–5627. https://doi.org/10.1073/pnas.1600108113.

(5) Lin-Moshier, Y.; Keebler, M. V.; Hooper, R.; Boulware, M. J.; Liu, X.; Churamani, D.; Abood, M. E.; Walseth, T. F.; Brailoiu, E.; Patel, S.; others. The Two-Pore Channel (TPC) Interactome Unmasks Isoform-Specific Roles for TPCs in Endolysosomal Morphology and Cell Pigmentation. *Proc. Natl. Acad. Sci.* **2014**, *111* (36), 13087–13092.

(6) García-Rúa, V.; Feijóo-Bandín, S.; Rodríguez-Penas, D.; Mosquera-Leal, A.; Abu-Assi, E.; Beiras, A.; María Seoane, L.; Lear, P.; Parrington, J.; Portolés, M.; Roselló-Lletí, E.; Rivera, M.; Gualillo, O.; Parra, V.; Hill, J. A.; Rothermel, B.; González-Juanatey, J. R.;

Lago, F. Endolysosomal Two-Pore Channels Regulate Autophagy in Cardiomyocytes. *J. Physiol.* **2016**, *594* (11), 3061–3077. https://doi.org/10.1113/JP271332.

(7) Pafumi, I.; Festa, M.; Papacci, F.; Lagostena, L.; Giunta, C.; Gutla, V.; Cornara, L.; Favia, A.; Palombi, F.; Gambale, F.; Filippini, A.; Carpaneto, A. Naringenin Impairs Two-Pore Channel 2 Activity And Inhibits VEGF-Induced Angiogenesis. *Sci. Rep.* **2017**, *7* (1), 5121. https://doi.org/10.1038/s41598-017-04974-1.

(8) Faviaa, A.; Desiderib, M.; Gambaraa, G.; D'Alessioa, A.; Ruas, M.; Esposito, B.; Bufalo, D. D.; Parrington, J.; Ziparoa, E.; Palombia, F.; Galioned, A.; Filippini, A. VEGF-Induced Neoangiogenesis Is Mediated by NAADP and Two-Pore Channel-2 -Dependent Ca2+signaling. *Proc. Natl. Acad. Sci. U. S. A.* **2014**, *111* (44), 4706–4715. https://doi.org/10.1073/pnas.1406029111.

(9) Wang, X.; Zhang, X.; Dong, X.; Samie, M.; Li, X.; Cheng, X.; Goschka, A.; Shen, D.; Zhou, Y.; Harlow, J.; others. TPC Proteins Are Phosphoinositide-Activated Sodium-Selective Ion Channels in Endosomes and Lysosomes. *Cell* **2012**, *151* (2), 372–383.

(10) Sakurai, Y.; Kolokoltsov, A. A.; Chen, C.-C.; Tidwell, M. W.; Bauta, W. E.; Klugbauer, N.; Grimm, C.; Wahl-Schott, C.; Biel, M.; Davey, R. A. Ebola Virus. Two-Pore Channels Control Ebola Virus Host Cell Entry and Are Drug Targets for Disease Treatment. *Science* **2015**, *347* (6225), 995–998. https://doi.org/10.1126/science.1258758.

(11) Gunaratne, G. S.; Yang, Y.; Li, F.; Walseth, T. F.; Marchant, J. S. NAADP-Dependent Ca2+ Signaling Regulates Middle East Respiratory Syndrome-Coronavirus Pseudovirus Translocation through the Endolysosomal System. *Cell Calcium* **2018**, *75*, 30–41. https://doi.org/10.1016/j.ceca.2018.08.003.

(12) Filippini, A.; D'Amore, A.; Palombi, F.; Carpaneto, A. Could the Inhibition of Endo-Lysosomal Two-Pore Channels (TPCs) by the Natural Flavonoid Naringenin Represent an Option to Fight SARS-CoV-2 Infection? *Front. Microbiol.* **2020**, *11*, 970. https://doi.org/10.3389/fmicb.2020.00970.

(13) Clementi, N.; Scagnolari, C.; D'Amore, A.; Palombi, F.; Criscuolo, E.; Frasca, F.; Pierangeli, A.; Mancini, N.; Antonelli, G.; Clementi, M.; Carpaneto, A.; Filippini, A. NARINGENIN IS A POWERFUL INHIBITOR OF SARS-CoV-2 INFECTION IN VITRO. *Pharmacol. Res.* **2020**, 105255. https://doi.org/10.1016/j.phrs.2020.105255.

(14) Ou, X.; Liu, Y.; Lei, X.; Li, P.; Mi, D.; Ren, L.; Guo, L.; Guo, R.; Chen, T.; Hu, J.; Xiang, Z.; Mu, Z.; Chen, X.; Chen, J.; Hu, K.; Jin, Q.; Wang, J.; Qian, Z. Characterization of Spike Glycoprotein of SARS-CoV-2 on Virus Entry and Its Immune Cross-Reactivity with SARS-CoV. *Nat. Commun.* **2020**, *11* (1), 1620–12. https://doi.org/10.1038/s41467-020-15562-9.

(15) Guo, J.; Zeng, W.; Chen, Q.; Lee, C.; Chen, L.; Yang, Y.; Cang, C.; Ren, D.; Jiang, Y. Structure of the Voltage-Gated Two-Pore Channel TPC1 from Arabidopsis Thaliana. *Nature* **2016**, *531* (7593), 196–201. https://doi.org/10.1038/nature16446.

(16) Guo, J.; Zeng, W.; Jiang, Y. Tuning the Ion Selectivity of Two-Pore Channels. *Proc. Natl. Acad. Sci. U. S. A.* **2017**, *114* (5), 1009–1014. https://doi.org/10.1073/pnas.1616191114.

(17) She, J.; Guo, J.; Chen, Q.; Zeng, W.; Jiang, Y.; Bai, X. Structural Insights into the Voltage and Phospholipid Activation of the Mammalian TPC1 Channel. *Nature* **2018**, *556* (7699), 130–134. https://doi.org/10.1038/nature26139.

(18) She, J.; Zeng, W.; Guo, J.; Chen, Q.; Bai, X.; Jiang, Y. Structural Mechanisms of Phospholipid Activation of the Human TPC2 Channel. *eLife* **2019**, *8*, 814. https://doi.org/10.7554/eLife.45222.

(19) Kintzer, A. F.; Stroud, R. M. On the Structure and Mechanism of Two-Pore Channels. *FEBS J.* **2017**. https://doi.org/10.1111/febs.14154.

(20) Costa, A.; Gutla, P. V. K.; Boccaccio, A.; Scholz-Starke, J.; Festa, M.; Basso, B.; Zanardi, I.; Pusch, M.; Schiavo, F. L.; Gambale, F.; Carpaneto, A. The Arabidopsis Central Vacuole as an Expression System for Intracellular Transporters: Functional

Characterization of the Cl-/H+ Exchanger CLC-7. *J. Physiol.* **2012**, *590* (15), 3421–3430. https://doi.org/10.1113/jphysiol.2012.230227.

(21) Boccaccio, A.; Scholz-Starke, J.; Hamamoto, S.; Larisch, N.; Festa, M.; Gutla, P. V. K.; Costa, A.; Dietrich, P.; Uozumi, N.; Carpaneto, A. The Phosphoinositide PI(3,5)P_2 Mediates Activation of Mammalian but Not Plant TPC Proteins: Functional Expression of Endolysosomal Channels in Yeast and Plant Cells. *Cell. Mol. Life Sci.* **2014**, *71* (21), 4275–4283. https://doi.org/10.1007/s00018-014-1623-2.

(22) Festa, M.; Lagostena, L.; Carpaneto, A. Using the Plant Vacuole as a Biological System to Investigate the Functional Properties of Exogenous Channels and Transporters. *Biochim. Biophys. Acta* **2016**, *1858* (3), 607–612. https://doi.org/10.1016/j.bbamem.2015.09.022.

(23) Kirsch, S. A.; Kugemann, A.; Carpaneto, A.; Böckmann, R. A.; Dietrich, P. Phosphatidylinositol-3,5-Bisphosphate Lipid-Binding-Induced Activation of the Human Two-Pore Channel 2. *Cell. Mol. Life Sci.* **2018**, *1851* (5), 1–13. https://doi.org/10.1007/s00018-018-2829-5.

(24) Hasegawa, J.; Strunk, B. S.; Weisman, L. S. PI5P and PI(3,5)P2: Minor, but Essential Phosphoinositides. *Cell Struct. Funct.* **2017**, *42* (1), 17003–17060. https://doi.org/10.1247/csf.17003.

(25) Benkerrou, D.; Minicozzi, V.; Gradogna, A.; Milenkovic, S.; Bodrenko, I. V.; Festa, M.; Lagostena, L.; Cornara, L.; D'Amore, A.; Ceccarelli, M.; Filippini, A.; Carpaneto, A. A Perspective on the Modulation of Plant and Animal Two Pore Channels (TPCs) by the Flavonoid Naringenin. *Biophys. Chem.* **2019**, *254*, 106246. https://doi.org/10.1016/j.bpc.2019.106246.

(26) D'Amore, A.; Gradogna, A.; Palombi, F.; Minicozzi, V.; Ceccarelli, M.; Carpaneto, A.; Filippini, A. The Discovery of Naringenin as Endolysosomal Two-Pore Channel Inhibitor and Its Emerging Role in SARS-CoV-2 Infection. *Cells* **2021**, *10* (5), 1130. https://doi.org/10.3390/cells10051130.

(27) Scholz-Starke, J.; Naso, A.; Carpaneto, A. A Perspective on the Slow Vacuolar Channel in Vacuoles from Higher Plant Cells, 2005.

(28) Gradogna, A.; Scholz-Starke, J.; Gutla, P. V. K.; Carpaneto, A. Fluorescence Combined with Excised Patch: Measuring Calcium Currents in Plant Cation Channels. *Plant J.* **2009**, *58* (1), 175–182.

(29) Carpaneto, A.; Gradogna, A. Modulation of Calcium and Potassium Permeation in Plant TPC Channels. *Biophys. Chem.* **2018**, *236*, 1–7. https://doi.org/10.1016/j.bpc.2018.02.006.

(30) Gerndt, S.; Chen, C.-C.; Chao, Y. K.; Yuan, Y.; Burgstaller, S.; Rosato, A. S.; Krogsaeter, E.; Urban, N.; Jacob, K.; Nguyen, O. N. P.; Miller, M. T.; Keller, M.; Vollmar, A. M.; Gudermann, T.; Zierler, S.; Schredelseker, J.; Schaefer, M.; Biel, M.; Malli, R.; Wahl-Schott, C.; Bracher, F.; Patel, S.; Grimm, C. Agonist-Mediated Switching of Ion Selectivity in TPC2 Differentially Promotes Lysosomal Function. *eLife* **2020**, *9*, 5622. https://doi.org/10.7554/eLife.54712.

(31) Gunaratne, G. S.; Brailoiu, E.; He, S.; Unterwald, E. M.; Patel, S.; Slama, J. T.; Walseth, T. F.; Marchant, J. S. Essential Requirement for JPT2 in NAADP-Evoked Ca2+ Signaling. *Sci. Signal.* **2021**, *14* (675). https://doi.org/10.1126/scisignal.abd5605.

(32) Milenkovic, S.; Bodrenko, I. V.; Lagostena, L.; Gradogna, A.; Serra, G.; Bosin, A.; Carpaneto, A.; Ceccarelli, M. The Mechanism and Energetics of a Ligand-Controlled Hydrophobic Gate in a Mammalian Two Pore Channel. *Phys. Chem. Chem. Phys. PCCP* **2020**, *22* (27), 15664–15674. https://doi.org/10.1039/d0cp00805b.

(33) Beckstein, O.; Biggin, P. C.; Sansom, M. S. A Hydrophobic Gating Mechanism for Nanopores. *J. Phys. Chem. B* **2001**, *105* (51), 12902–12905.

(34) Beckstein, O.; Biggin, P. C.; Bond, P.; Bright, J. N.; Domene, C.; Grottesi, A.; Holyoake, J.; Sansom, M. S. P. Ion Channel Gating: Insights via Molecular Simulations, 2003.
(35) Beckstein, O.; Sansom, M. S. P. A Hydrophobic Gate in an Ion Channel: The Closed State of the Nicotinic Acetylcholine Receptor. *Phys. Biol.* **2006**, *3* (2), 147. https://doi.org/10.1088/1478-3975/3/2/007.
(36) Bezanilla, F. Gating Currents. *J. Gen. Physiol.* **2018**, *150* (7), 911–932. https://doi.org/10.1085/jgp.201812090.
(37) Jin, X.; Zhang, Y.; Alharbi, A.; Hanbashi, A.; Alhoshani, A.; Parrington, J. Targeting Two-Pore Channels: Current Progress and Future Challenges. *Trends Pharmacol. Sci.* **2020**, *41* (8), 582–594. https://doi.org/10.1016/j.tips.2020.06.002.
(38) Aksimentiev, A.; Schulten, K. Imaging α-Hemolysin with Molecular Dynamics: Ionic Conductance, Osmotic Permeability, and the Electrostatic Potential Map. *Biophys. J.* **2005**, *88* (6), 3745–3761. https://doi.org/10.1529/biophysj.104.058727.
(39) Xu, H.; Ren, D. Lysosomal Physiology. In *Annual Review of Physiology*; University of Michigan, Ann Arbor, Ann Arbor, United States, 2015; pp 57–80. https://doi.org/10.1146/annurev-physiol-021014-071649.
(40) Chakrabarti, N.; Ing, C.; Payandeh, J.; Zheng, N.; Catterall, W. A.; Pomès, R. Catalysis of Na+ Permeation in the Bacterial Sodium Channel Na(V)Ab. *Proc. Natl. Acad. Sci.* **2013**, *110* (28), 11331–11336. https://doi.org/10.1073/pnas.1309452110.
(41) Furini, S.; Domene, C. K(+) and Na(+) Conduction in Selective and Nonselective Ion Channels via Molecular Dynamics Simulations. *Biophys. J.* **2013**, *105* (8), 1737–1745. https://doi.org/10.1016/j.bpj.2013.08.049.
(42) Furini, S.; Domene, C. Computational Studies of Transport in Ion Channels Using Metadynamics. *Biochim. Biophys. Acta BBA-Biomembr.* **2016**, *1858* (7), 1733–1740. https://doi.org/10.1016/j.bbamem.2016.02.015.
(43) Furini, S.; Domene, C. Gating at the Selectivity Filter of Ion Channels That Conduct Na + and K + Ions. *Biophys. J.* **2011**, *101* (7), 1623–1631. https://doi.org/10.1016/j.bpj.2011.08.035.
(44) Richards, L. A.; Schäfer, A. I.; Richards, B. S.; Corry, B. The Importance of Dehydration in Determining Ion Transport in Narrow Pores. *Small* **2012**, *8* (11), 1701–1709. https://doi.org/10.1002/smll.201102056.
(45) Köpfer, D. A.; Song, C.; Gruene, T.; Sheldrick, G. M.; Zachariae, U.; de Groot, B. L. Ion Permeation in K+ Channels Occurs by Direct Coulomb Knock-On. *Science* **2014**, *346* (6207), 352–355. https://doi.org/10.1126/science.1254840.
(46) Ballabio, A.; Bonifacino, J. S. Lysosomes as Dynamic Regulators of Cell and Organismal Homeostasis. *Nat. Rev. Mol. Cell Biol.* **2020**, 1–18. https://doi.org/10.1038/s41580-019-0185-4.
(47) Nekolla, S.; Andersen, C.; Benz, R. Noise Analysis of Ion Current through the Open and the Sugar-Induced Closed State of the LamB Channel of Escherichia Coli Outer Membrane: Evaluation of the Sugar Binding Kinetics to the Channel Interior. *Biophys. J.* **1994**, *66* (5), 1388–1397. https://doi.org/10.1016/S0006-3495(94)80929-4.
(48) Tang, L.; El-Din, T. M. G.; Payandeh, J.; Martinez, G. Q.; Heard, T. M.; Scheuer, T.; Zheng, N.; Catterall, W. A. Structural Basis for Ca 2+ Selectivity of a Voltage-Gated Calcium Channel. *Nat. Publ. Group* **2014**, *505* (7481), 56–61. https://doi.org/10.1038/nature12775.
(49) Saotome, K.; Singh, A. K.; Yelshanskaya, M. V.; Sobolevsky, A. I. Crystal Structure of the Epithelial Calcium Channel TRPV6. *Nat. Publ. Group* **2016**, *534* (7608), 506–511. https://doi.org/10.1038/nature17975.
(50) Sakipov, S.; Sobolevsky, A. I.; Kurnikova, M. G. Ion Permeation Mechanism in Epithelial Calcium Channel TRVP6. *Sci. Rep.* **2018**, 1–13. https://doi.org/10.1038/s41598-018-23972-5.

(51) Pohorille, A.; Wilson, M. A.; Wei, C. Validity of the Electrodiffusion Model for Calculating Conductance of Simple Ion Channels. *J. Phys. Chem. B* **2017**, *121* (15), 3607–3619. https://doi.org/10.1021/acs.jpcb.6b09598.
(52) Levitt, D. G. Interpretation of Biological Ion Channel Flux Data--Reaction-Rate versus Continuum Theory. *Annu. Rev. Biophys. Biophys. Chem.* **1986**, *15*, 29–57. https://doi.org/10.1146/annurev.bb.15.060186.000333.
(53) Cooper, K. E.; Gates, P. Y.; Eisenberg, R. S. Diffusion Theory and Discrete Rate Constants in Ion Permeation. *J. Membr. Biol.* **1988**, *106* (2), 95–105. https://doi.org/10.1007/BF01871391.
(54) Coines, J.; Acosta-Gutierrez, S.; Bodrenko, I.; Rovira, C.; Ceccarelli, M. Glucose Transport via the Pseudomonad Porin OprB: Implications for the Design of Trojan Horse Anti-Infectives. *Phys. Chem. Chem. Phys. PCCP* **2019**, *14* (16), 529–8463. https://doi.org/10.1039/c9cp00778d.
(55) Pira, A.; Scorciapino, M. A.; Bodrenko, I. V.; Bosin, A.; Acosta-Gutierrez, S.; Ceccarelli, M. Permeation of β-Lactamase Inhibitors through the General Porins of Gram-Negative Bacteria. *Molecules* **2020**, *25* (23), 5747. https://doi.org/10.3390/molecules25235747.
(56) Zhao, Z.; Qin, P.; Huang, Y.-W. Lysosomal Ion Channels Involved in Cellular Entry and Uncoating of Enveloped Viruses: Implications for Therapeutic Strategies against SARS-CoV-2. **2021**, 1–7. https://doi.org/10.1016/j.ceca.2021.102360.
(57) Zhekova, H. R.; Van Ngo; da Silva, M. C.; Salahub, D.; Noskov, S. Selective Ion Binding and Transport by Membrane Proteins Â€“ A Computational Perspective. **2017**, 1–29. https://doi.org/10.1016/j.ccr.2017.03.019.
(58) Ren, D.; Navarro, B.; Xu, H.; Yue, L.; Shi, Q.; Clapham, D. E. A Prokaryotic Voltage-Gated Sodium Channel. *Science* **2001**, *294* (5550), 2372–2375. https://doi.org/10.1126/science.1065635.
(59) HILLE, B.; SCHWARZ, W. POTASSIUM CHANNELS AS MULTI-ION SINGLE-FILE PORES. *J. Gen. Physiol.* **1978**, *72* (4), 409–442.
(60) Coutsias, E. A.; Seok, C.; Jacobson, M. P.; Dill, K. A. A Kinematic View of Loop Closure. *J Comput Chem* **2004**, *25* (4), 510–528. https://doi.org/10.1002/jcc.10416.
(61) Wu, E. L.; Cheng, X.; Jo, S.; Rui, H.; Song, K. C.; Dávila-Contreras, E. M.; Qi, Y.; Lee, J.; Monje-Galvan, V.; Venable, R. M.; others. CHARMM-GUI Membrane Builder toward Realistic Biological Membrane Simulations. *J. Comput. Chem.* **2014**, *35* (27), 1997–2004.
(62) Jo, S.; Lim, J. B.; Klauda, J. B.; Im, W. CHARMM-GUI Membrane Builder for Mixed Bilayers and Its Application to Yeast Membranes. *Biophys. J.* **2009**, *97* (1), 50–58.
(63) Brooks, B. R.; Brooks III, C. L.; MacKerell Jr., A. D.; Nilsson, L.; Petrella, R. J.; Roux, B.; Won, Y.; Archontis, G.; Bartels, C.; Boresch, S.; others. CHARMM: The Biomolecular Simulation Program. *J. Comput. Chem.* **2009**, *30* (10), 1545–1614.
(64) Lee, J.; Cheng, X.; Swails, J. M.; Yeom, M. S.; Eastman, P. K.; Lemkul, J. A.; Wei, S.; Buckner, J.; Jeong, J. C.; Qi, Y.; others. CHARMM-GUI Input Generator for NAMD, GROMACS, AMBER, OpenMM, and CHARMM/OpenMM Simulations Using the CHARMM36 Additive Force Field. *J. Chem. Theory Comput.* **2016**, *12* (1), 405–413.
(65) Berendsen, H. J. C.; van der Spoel, D.; van Drunen, R. GROMACS: A Message-Passing Parallel Molecular Dynamics Implementation. *Comput. Phys. Commun.* **1995**, *91* (1–3), 43–56. https://doi.org/10.1016/0010-4655(95)00042-E.
(66) Lindahl, E.; Hess, B.; Van Der Spoel, D. GROMACS 3.0: A Package for Molecular Simulation and Trajectory Analysis. *J. Mol. Model.* **2001**, *7* (8), 306–317. https://doi.org/10.1007/S008940100045.
(67) Van Der Spoel, D.; Lindahl, E.; Hess, B.; Groenhof, G.; Mark, A. E.; Berendsen, H. J. C. GROMACS: Fast, Flexible, and Free. *J Comput Chem* **2005**, *26* (16), 1701–1718. https://doi.org/10.1002/jcc.20291.

(68) Hess, B.; Kutzner, C.; Van Der Spoel, D.; Lindahl, E. GRGMACS 4: Algorithms for Highly Efficient, Load-Balanced, and Scalable Molecular Simulation. *J. Chem. Theory Comput.* **2008**, *4* (3), 435–447. https://doi.org/10.1021/ct700301q.

(69) Pronk, S.; Páll, S.; Schulz, R.; Larsson, P.; Bjelkmar, P.; Apostolov, R.; Shirts, M. R.; Smith, J. C.; Kasson, P. M.; Van Der Spoel, D.; Hess, B.; Lindahl, E. GROMACS 4.5: A High-Throughput and Highly Parallel Open Source Molecular Simulation Toolkit. *Bioinforma. Oxf. Engl.* **2013**, *29* (7), 845–854. https://doi.org/10.1093/bioinformatics/btt055.

(70) Abraham, M. J.; Murtola, T.; Schulz, R.; Páll, S.; Smith, J. C.; Hess, B.; Lindah, E. Gromacs: High Performance Molecular Simulations through Multi-Level Parallelism from Laptops to Supercomputers. *SoftwareX* **2015**, *1–2*, 19–25. https://doi.org/10.1016/j.softx.2015.06.001.

(71) Best, R. B.; Zhu, X.; Shim, J.; Lopes, P. E.; Mittal, J.; Feig, M.; MacKerell Jr., A. D. Optimization of the Additive CHARMM All-Atom Protein Force Field Targeting Improved Sampling of the Backbone ϕ, ψ and Side-Chain X1 and X2 Dihedral Angles. *J. Chem. Theory Comput.* **2012**, *8* (9), 3257–3273.

(72) Mackerell, A. D.; Bashford, D.; Bellott, M.; Dunbrack, R. L.; Evanseck, J. D.; Field, M. J.; Fischer, S.; Gao, J.; Guo, H.; Ha, S.; Joseph-McCarthy, D.; Kuchnir, L.; Kuczera, K.; Lau, F. T. K.; Mattos, C.; Michnick, S.; Ngo, T.; Nguyen, D. T.; Prodhom, B.; Reiher, W. E.; Roux, B.; Schlenkrich, M.; Smith, J. C.; Stote, R.; Straub, J.; Watanabe, M.; Wiórkiewicz-Kuczera, J.; Yin, D.; Karplus, M. All-Atom Empirical Potential for Molecular Modeling and Dynamics Studies of Proteins. *J. Phys. Chem. B* **1998**, *102* (18), 3586–3616.

(73) Huang, J.; Rauscher, S.; Nawrocki, G.; Ran, T.; Feig, M.; de Groot, B. L.; Grubmüller, H.; Mackerell, A. D. CHARMM36m: An Improved Force Field for Folded and Intrinsically Disordered Proteins. *Nat. Methods* **2017**, *14* (1), 71–73. https://doi.org/10.1038/nmeth.4067.

(74) Mackerell, A. D.; Feig, M.; Brooks, C. L. Extending the Treatment of Backbone Energetics in Protein Force Fields: Limitations of Gas-Phase Quantum Mechanics in Reproducing Protein Conformational Distributions in Molecular Dynamics Simulation. *J Comput Chem* **2004**, *25* (11), 1400–1415. https://doi.org/10.1002/jcc.20065.

(75) Klauda, J. B.; Venable, R. M.; Freites, J. A.; O'Connor, J. W.; Tobias, D. J.; Mondragon-Ramirez, C.; Vorobyov, I.; MacKerell Jr., A. D.; Pastor, R. W. Update of the CHARMM All-Atom Additive Force Field for Lipids: Validation on Six Lipid Types. *J. Phys. Chem. B* **2010**, *114* (23), 7830–7843. https://doi.org/10.1021/jp101759q.

(76) Jorgensen, W. L.; Chandrasekhar, J.; Madura, J. D.; Impey, R. W.; Klein, M. L. Comparison of Simple Potential Functions for Simulating Liquid Water. *J. Chem. Phys.* **1983**, *79* (2), 926. https://doi.org/10.1063/1.445869.

(77) Vanommeslaeghe, K.; Hatcher, E.; Acharya, C.; Kundu, S.; Zhong, S.; Shim, J.; Darian, E.; Guvench, O.; Lopes, P.; Vorobyov, I.; Mackerell, A. D. CHARMM General Force Field: A Force Field for Drug-like Molecules Compatible with the CHARMM All-Atom Additive Biological Force Fields. *J Comput Chem* **2010**, *31* (4), 671–690. https://doi.org/10.1002/jcc.21367.

(78) Berendsen, H. J. C.; Postma, J. P. M.; van Gunsteren, W. F.; Dinola, A.; Haak, J. R. Molecular Dynamics with Coupling to an External Bath. *J. Chem. Phys.* **1984**, *81* (8), 3684–3690. https://doi.org/10.1063/1.448118.

(79) Bussi, G.; Donadio, D.; Parrinello, M. Canonical Sampling through Velocity Rescaling. *J. Chem. Phys.* **2007**, *126* (1), 014101. https://doi.org/10.1063/1.2408420.

(80) Perera, L.; Essmann, U.; Berkowitz, M. L. Effect of the Treatment of Long-range Forces on the Dynamics of Ions in Aqueous Solutions. *J. Chem. Phys.* **1995**, *102* (1), 450–456. https://doi.org/10.1063/1.469422.

(81) Mironenko, A.; Zachariae, U.; de Groot, B. L.; Kopec, W. The Persistent Question of Potassium Channel Permeation Mechanisms. *J. Mol. Biol.* **2021**, 167002. https://doi.org/10.1016/j.jmb.2021.167002.
(82) Venable, R. M.; Luo, Y.; Gawrisch, K.; Roux, B.; Pastor, R. W. Simulations of Anionic Lipid Membranes: Development of Interaction-Specific Ion Parameters and Validation Using NMR Data. *J. Phys. Chem. B* **2013**, *117* (35), 10183–10192. https://doi.org/10.1021/jp401512z.
(83) Savelyev, A.; Mackerell, A. D. Competition among Li+, Na+, K+, and Rb+ Monovalent Ions for DNA in Molecular Dynamics Simulations Using the Additive CHARMM36 and Drude Polarizable Force Fields. *J. Phys. Chem. B* **2015**, *119* (12), 4428–4440. https://doi.org/10.1021/acs.jpcb.5b00683.
(84) Han, K.; Venable, R. M.; Bryant, A. M.; Legacy, C. J.; Shen, R.; Li, H.; Roux, B.; Gericke, A.; Pastor, R. W. Graph-Theoretic Analysis of Monomethyl Phosphate Clustering in Ionic Solutions. *J. Phys. Chem. B* **2018**, *122* (4), 1484–1494. https://doi.org/10.1021/acs.jpcb.7b10730.
(85) Gumbart, J.; Khalili-Araghi, F.; Sotomayor, M.; Roux, B. Constant Electric Field Simulations of the Membrane Potential Illustrated with Simple Systems. *Biochim. Biophys. Acta* **2012**, *1818* (2), 294–302. https://doi.org/10.1016/j.bbamem.2011.09.030.
(86) Tribello, G. A.; Bonomi, M.; Branduardi, D.; Camilloni, C.; Bussi, G. PLUMED 2: New Feathers for an Old Bird. *Comput. Phys. Commun.* **2014**, *185* (2), 604–613. https://doi.org/10.1016/j.cpc.2013.09.018.
(87) Barducci, A.; Bussi, G.; Parrinello, M. Well-Tempered Metadynamics: A Smoothly Converging and Tunable Free-Energy Method. *Phys. Rev. Lett.* **2008**, *100* (2), 1–4. https://doi.org/10.1103/PhysRevLett.100.020603.
(88) Bonomi, M.; Barducci, A.; Parrinello, M. Reconstructing the Equilibrium Boltzmann Distribution from Well-Tempered Metadynamics. *J. Comput. Chem.* **2009**, *30* (11), 1615–1621.
(89) Branduardi, D.; Bussi, G.; Parrinello, M.; 2012. Metadynamics with Adaptive Gaussians. *J. Chem. Theory Comput. 8*, 2247–2254. https://doi.org/10.1021/ct3002464.
(90) Ghai, I.; Pira, A.; Scorciapino, M. A.; Bodrenko, I.; Benier, L.; Ceccarelli, M.; Winterhalter, M.; Wagner, R. General Method to Determine the Flux of Charged Molecules through Nanopores Applied to β-Lactamase Inhibitors and OmpF. *J. Phys. Chem. Lett.* **2017**, *8* (6), 1295–1301. https://doi.org/10.1021/acs.jpclett.7b00062.
(91) Kumar, A.; Hajjar, E.; Ruggerone, P.; Ceccarelli, M. Structural and Dynamical Properties of the Porins OmpF and OmpC: Insights from Molecular Simulations. *J. Phys. Condens. Matter* **2010**, *22* (45), 454125. https://doi.org/10.1088/0953-8984/22/45/454125.

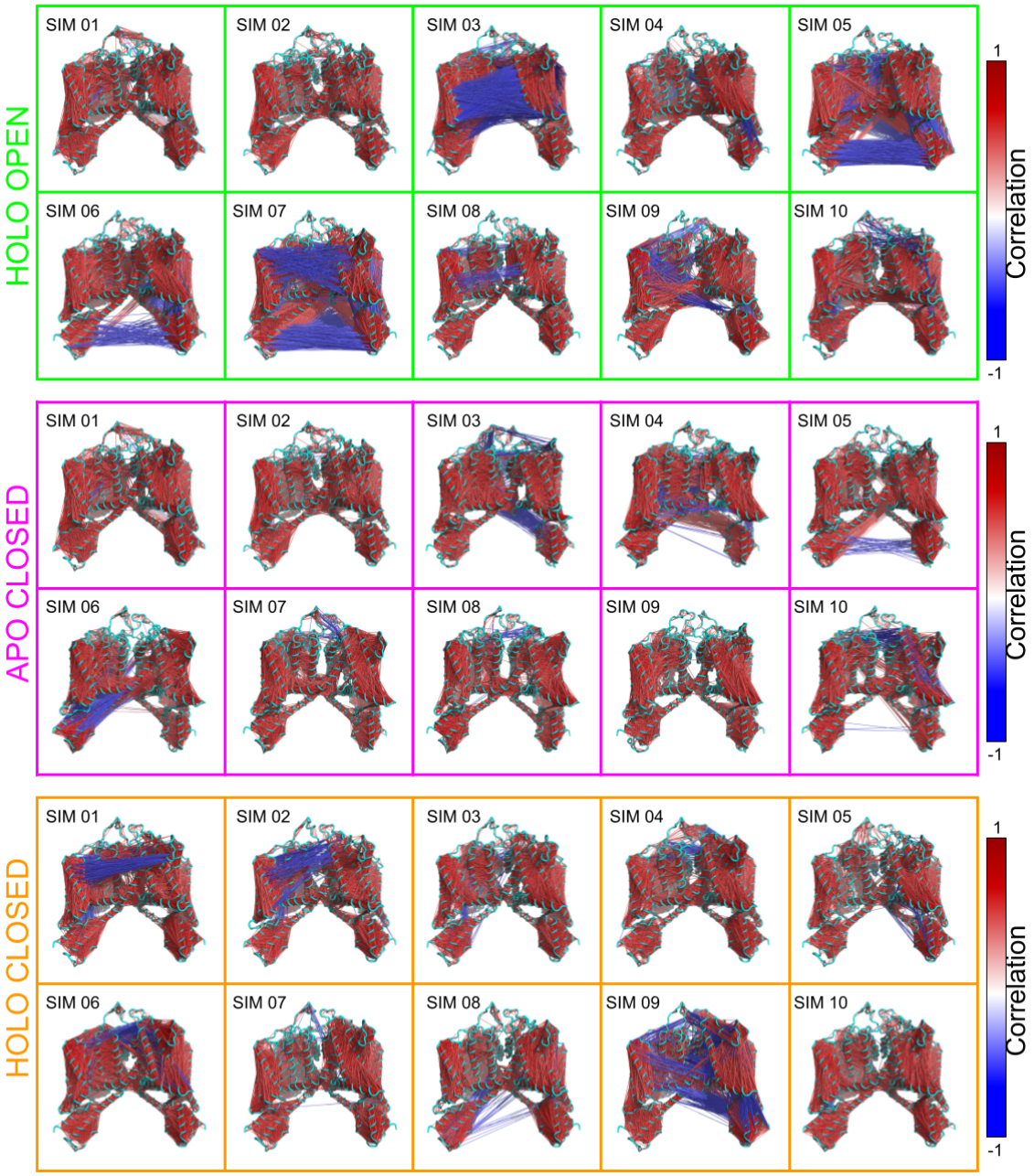

SI 1. The molecular graphics of significant (<0.6) Cα-Cα cross-correlation in three systems holoO, apoC, and holoC shown for each independent trajectory.

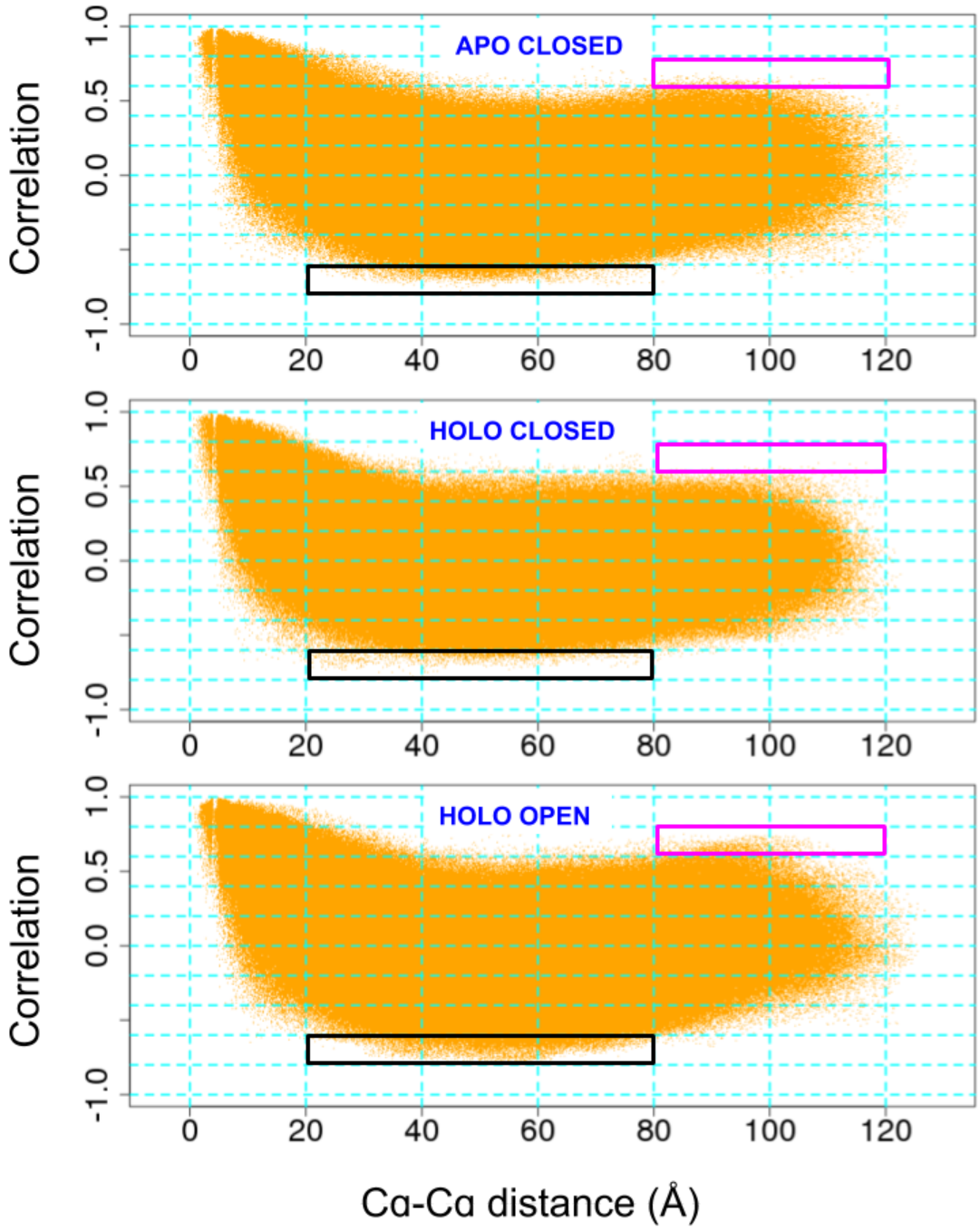

SI 2. The Cα-Cα cross-correlation in three systems apoC, holoC and holoO plotted against corresponding Cα-Cα average distances. The regions of interest are highlighted with black and magenta rectangles.

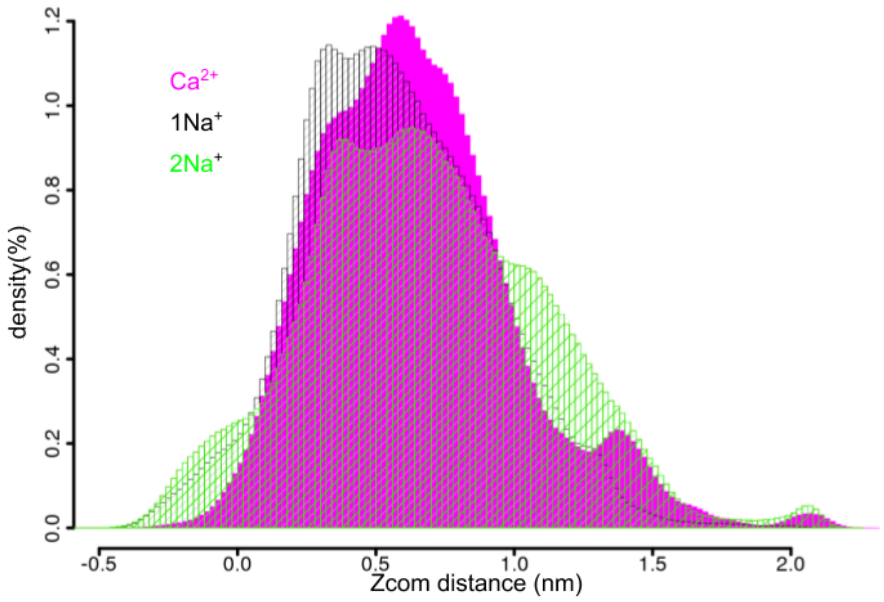

SI 3. Histograms of the Z-component of the center of mass distance between the ion(s) kept inside the cavity during the MTD simulations: MTD_Ca^{2+}(magenta), MTD_Na^{1+}(black-shaded bars) and MTD_2Na^{1+}(green-shaded bars).

1. Free energy decomposition in occupancy contributions.

We consider a channel that can be occupied by more than one substrate, e.g. ions. In a NVT ensemble containing $N + 1$ions, we consider one specific ion (ion "0") and limit its motion by a repulsive cylinder of radius $R$and length L oriented along the channel (z) and centered at the COM of the channel. All the other particles do not see (do not interact with) the cylinder.

We consider the probability, q_i, of $i(= 0, 1, 2)$occupation number (occupancy) of the pore central region Ω by any ion, and the conditional probability density, $P(z|i)$, for the ion "0" to be in position z at the condition of the $i(= 0, 1, 2)$specific ions are in Ω.

The occupancies, q_i, can be calculated in the plain MD simulations by counting the events in which the cavity has a certain occupation number and dividing it by the total length of the simulation. The conditional probabilities, $P(z|i)$, require much longer trajectories in plain MD. These can be more readily calculated by using an enhanced sampling method, e.g. the metadynamics, where ion "0" is biased. We consider three free energy profiles for ion "0": $G_0(z)$- when no other ion is allowed to enter the pore central region Ω; $G_1(z)$ - when another specific ion (ion "1") is always kept in region Ω; $G_2(z)$- when the two specific ions (ions "1" and "2") are kept in region Ω. Then, one obtains,

$$P(z|i) = \frac{\exp\left(-G_i(z)/kT\right)}{\int \exp\left(-G_i(x)/kT\right)dx}. \quad (1)$$

The "reconstructed" unrestricted probability density, $p(z)$, and the corresponding free energy profile, $G(z)$, was obtained as follows,

$$p(z) \propto \exp(-\ G(z)/kT) = A\sum_i \frac{\exp\left(-G_i(z)/kT\right)}{\int \exp\left(-G_i(x)/kT\right)dx}\frac{q_i}{g_i} \quad (2)$$

where g_i is the statistical combinatorial factor giving the number of options to select $i(=0,1,2)$ions out of Nfixed in regionΩ,

$$g_0 = 1; \quad g_1 = N; \quad g_2 = \frac{N(N-1)}{2}. \quad (3)$$

The normalization constants, A, was selected to set the free energy to zero outside the channel.

2. Error calculations for metadynamics free energy surfaces

We calculated the error for each free energy surface as the difference between the free energy obtained summing up the accumulated hills (F(s,T)) and the free energy obtained directly from the sampled values of the collective variable s accumulated during metadynamics simulations, up to time T (F_N(s,T)). While hills are added with a frequency of 5 ps, the variable s is stored for each walker with a higher frequency, 1 ps. The accumulated histogram calculated from the walker trajectories, weighted with the relative bias factor, represents a free-energy estimator, as discussed in Ref. 1 and 2.

In figure SI4 we reported for each metadynamics simulation the F(s,T) and the F_N(s,T), the former with straight lines and the latter with dotted lines. As we can see, though there are some differences, the use of the free-energy estimator does not change qualitatively our results.

The average error among the two curves is obtained with the formula (22) of Ref. 1, without excluding any points.

$$\varepsilon = \left[\frac{\int_s [\overline{F_r}(s) - \overline{F}\ (s)]^2 \theta(\nu - F_r(s))ds}{\int_s \theta(\nu - F_r(s))ds}\right]^{1/2}$$

1. Branduardi D., Bussi, G., Parrinello, M.2012. Metadynamics with adaptive Gaussians. Journal of Chemical Theory and Computation 8, 2247–2254 and
2. Barducci, A.; Bussi, G.; Parrinello, M. Phys. Rev. Lett. 2008, 100,020603.

SI 4:

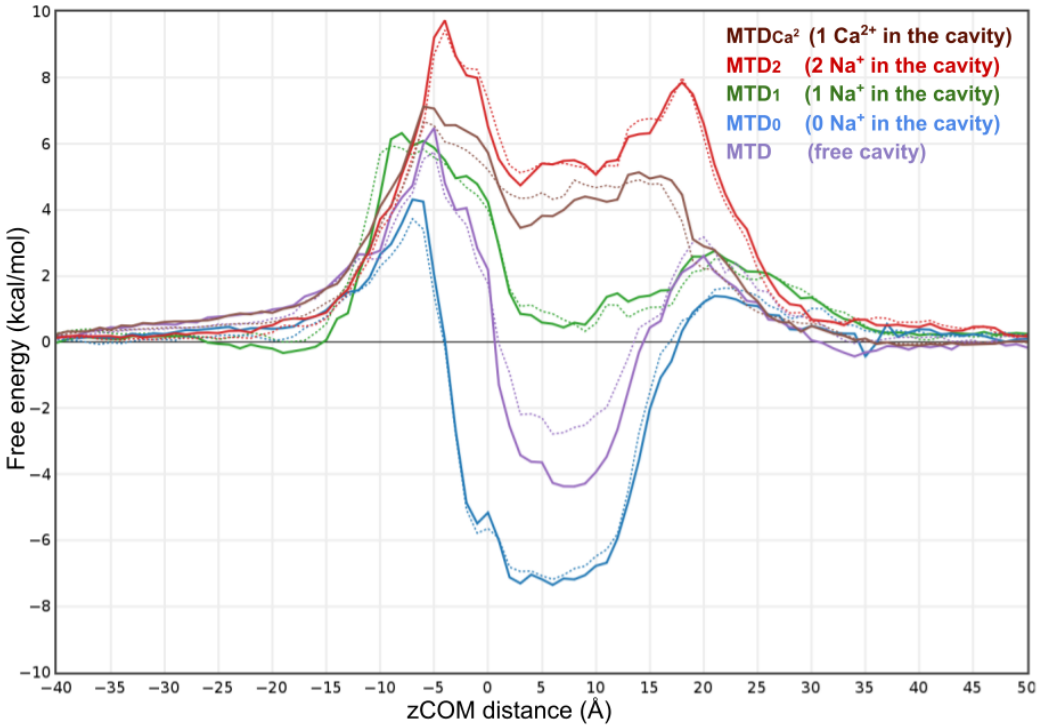

SI4. The free energy profiles of various MTD simulations (solid lines) accompanied by their F_N counterparts (dashed lines), as described above.

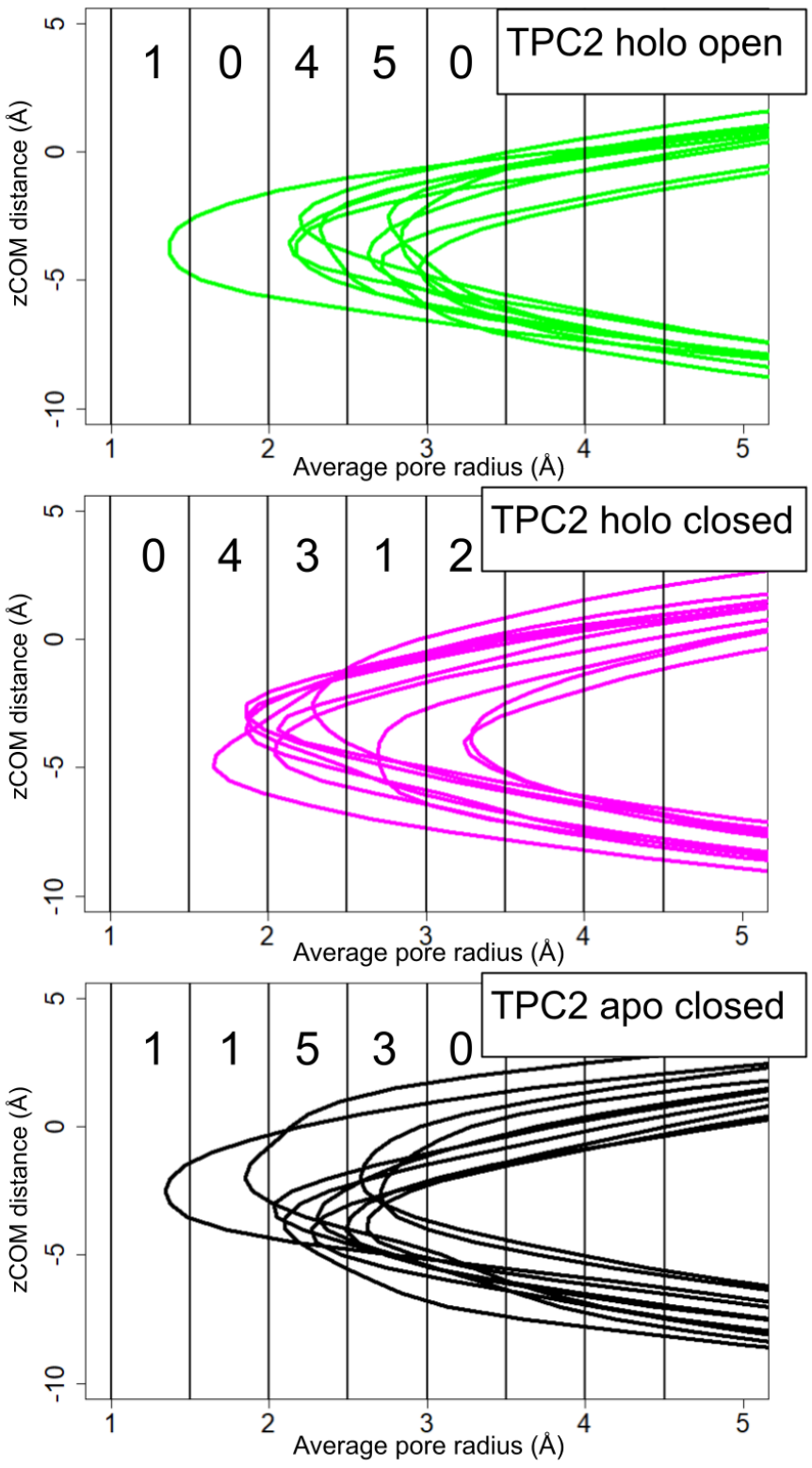

SI 5. Average pore radius profiles for different simulations. The counts of their minimal values are given for 0.5 angstrom bin at the top of each panel.

#x300 ns	Ion dynamics with the time of the entry, time of the exit and the life time inside the cavity.												
1	t_1(in) =0	t_1(out) =34.6	τ_1 =35	t_2(in) =35.4	t_2(out) =38.9	τ_2 =3.4	t_3(in) =38.3	t_3(out) =100.2	τ_3 =62	t_4(in) =96	t_4(out) =168.1	τ_4 =72	t_5(in) =160.1
2	t_5(out) =440	τ_5 =280	t_6(in) =467.1										
3	t_6(out) =667	τ_6 =200											
4	t_7(in) =981												
5	t_7(out) =1400	τ_7 =419	t_8(in) =1394	t_8(out) =1414	τ_8 =20	t_9(in) =1446							
6	t_9(out) =1523	τ_9 =77	t_{10}(in) =1527										
7	t_{10}(out) =2099	τ_{10} =570											
8	t_{11}(in) =2147												
9													
10													

SI TABLE 1. The timeline of ion passages in the long 3us simulation. Each ion is described with three fields, time of entry, time of exit and the time spent inside the cavity. The exception is the last ion which doesn't leave the cavity for the time of the simulation.

Cavity state	Zero ions	Single ion	Two ions
holoO MD	38%	60%	2%
holoO -200mV	10%	85%	5%
holoO MTD	23%	75%	2%

SI TABLE 2. The ion occupancy for three different types of holoO simulations.

TOC: the central cavity of hTPC2 works as a reservoir of sodium ions and its occupation modulates the ionic current